



Constructing Floor Plan through Smoke Using Ultra Wideband Radar

WEIYAN CHEN, Peking University, China

FUSANG ZHANG, Nanjing University and Institute of Software, Chinese Academy of Sciences, China

TAO GU, Macquarie University, Australia

KEXING ZHOU, Peking University, China

ZIXUAN HUO, Peking University, China

DAQING ZHANG*, Peking University, China and Institut Polytechnique de Paris, France

Floor plan construction has been one of the key techniques in many important applications such as indoor navigation, location-based services, and emergency rescue. Existing floor plan construction methods require expensive dedicated hardware (e.g., Lidar or depth camera), and may not work in low-visibility environments (e.g., smoke, fog or dust). In this paper, we develop a low-cost Ultra Wideband (UWB)-based system (named UWBMap) that is mounted on a mobile robot platform to construct floor plan through smoke. UWBMap leverages on low-cost and off-the-shelf UWB radar, and it is able to construct an indoor map with an accuracy comparable to Lidar (i.e., the state-of-the-art). The underpinning technique is to take advantage of the mobility of radar to form virtual antennas and gather spatial information of a target. UWBMap also eliminates both robot motion noise and environmental noise to enhance weak reflection from small objects for the robust construction process. In addition, we overcome the limited view of single radar by combining multi-view from multiple radars. Extensive experiments in different indoor environments show that UWBMap achieves a map construction with a median error of 11 cm and a 90-percentile error of 26 cm, and it operates effectively in indoor scenarios with glass wall and dense smoke.

CCS Concepts: • Human-centered computing → Ubiquitous and mobile computing systems and tools.

Additional Key Words and Phrases: IR-UWB Radar, Floor Plan Construction, Indoor Mapping, Multiple View, See through Smoke

ACM Reference Format:

Weiyan Chen, Fusang Zhang, Tao Gu, Kexing Zhou, Zixuan Huo, and Daqing Zhang. 2021. Constructing Floor Plan through Smoke Using Ultra Wideband Radar. *Proc. ACM Interact. Mob. Wearable Ubiquitous Technol.* 5, 4, Article 147 (December 2021), 29 pages. <https://doi.org/10.1145/3494977>

*Corresponding author

Authors' addresses: Weiyan Chen, chenwy1117@pku.edu.cn, Key Laboratory of High Confidence Software Technologies (Ministry of Education), School of Electronics Engineering and Computer Science, Peking University, Beijing, P.R China. Fusang Zhang, zhangfusang @otcaix.icscas.ac.cn, State Key Laboratory for Novel Software Technology, Nanjing University, Nanjing, P.R China; State Key Laboratory of Computer Sciences, Institute of Software, Chinese Academy of Sciences, Beijing, P.R China. Tao Gu, tao.gu@mq.edu.au, Department of Computing, Macquarie University, Australia. Kexing Zhou, KEKE_046@pku.edu.cn; Zixuan Huo, hzx20000818@gmail.com, School of Electronics Engineering and Computer Science, Peking University, Beijing, P.R China. Daqing Zhang, dqzhang@sei.pku.edu.cn, Key Laboratory of High Confidence Software Technologies (Ministry of Education), School of Electronics Engineering and Computer Science, Peking University, Beijing, China, Département Réseaux et Services Multimédia Mobiles, Institut Polytechnique de Paris, Evry, France.

Permission to make digital or hard copies of all or part of this work for personal or classroom use is granted without fee provided that copies are not made or distributed for profit or commercial advantage and that copies bear this notice and the full citation on the first page. Copyrights for components of this work owned by others than ACM must be honored. Abstracting with credit is permitted. To copy otherwise, or republish, to post on servers or to redistribute to lists, requires prior specific permission and/or a fee. Request permissions from permissions@acm.org.

© 2021 Association for Computing Machinery.

2474-9567/2021/12-ART147 \$15.00

<https://doi.org/10.1145/3494977>

1 INTRODUCTION

Constructing floor plan is important to search and rescue in disaster events such as building fires. Knowing the floor plan in an event building will enable rescuers to choose the best path and execute the rescue plan efficiently. However, the floor plans of a building may not be available under harsh conditions, and they may be changed from original maps due to collapse of building structures. Navigating in an event building without an accurate floor plan can be threatened to rescuer's life and delay rescue.

Mobile robots equipped with mapping devices have been used to measure indoor floor plans. Table 1 summarizes and compares the state-of-the-art floor mapping platforms. They typically use optical sensors to obtain indoor maps in detail, such as laser range scanners (Lidar) [10, 44, 45], depth cameras [28, 51] and RGB cameras [16, 19]. While they achieve promising accuracy, Lidar is expensive and does not work on transparent materials (i.e., glass) that are commonly seen in indoor settings. Camera-based approaches passively capture light scattered by surrounding objects. They are sensitive to lighting conditions that may become unstable during a disaster event. Moreover, the performance of optical-sensor based systems can be seriously affected in the presence of airborne obstacles such as smoke and dust, in the worst case leading to malfunction. Acoustic-based approaches such as microphones [32, 53] and ultrasonic sensors [12] are robust to ambient lighting conditions and transparent materials, but they have a limited sensing range and lack the ability of working effectively in noisy environments.

Radar devices such as millimeter Wave (mmWave) radar and Impulse-Radio Ultra-Wideband (IR-UWB) radar have recently become popular for indoor ranging and sensing applications. They actively transmit RF signals and process the reflections to sense nearby objects' range, speed or angle, hence they can be used indoors under adverse environmental conditions such as poor lighting and smoke. MmWave radars have been used in several domains such as automotive [42], human sensing [3] and floor plan construction [15, 30]. However, mmWave radars work in a higher frequency band (e.g., 77GHz) and have a shorter wavelength (4mm), hence they have higher energy attenuation over distance and weaker penetrability through walls. Different from mmWave radars, the frequency band of IR-UWB radars is much lower (i.e., 3.1GHz ~ 10.6GHz), the miniaturization of IR-UWB radar has significantly reduced its weight, cost and energy consumption (i.e., in mW level [4]). IR-UWB radar has been incorporated into many commercial smartphones (e.g., iphone 12 [23] and Galaxy Note 20 [37]) and mobile robots. Compared with off-the-shelf mmWave radars such as TI's AWR1642 [25] and AWR1443 [24] which usually cost hundreds of dollars, the cost of IR-UWB radar for mass order can be as low as tens of dollars and its power consumption is only one-tenth that of mmWave radar. IR-UWB radar has its cost advantage for a wider range of applications.

The basic idea of floor plan construction is scanning each part of the room with different ranges and angles, acquiring the information for each scan, and combining them into a complete image (i.e., layout). A building layout is composed of different contours of objects, we name each part of the room as *target*.

However, it is not a trivial task to achieve reliable IR-UWB based floor plan construction in adverse indoor environments. Several challenges exist. Firstly, angle resolution is crucial to distinguish multiple targets from a single scan. Different from Lidar which has narrow light beam, an IR-UWB radar has wider beam and weak directivity. As a result, IR-UWB radar may not reach angle resolution as in Lidar. A single mono-static radar is not able to identify the spatial position of a target. Deploying more antennas can improve directivity of radio frequency (RF) signal, however, it comes at a high cost and may not be feasible for commercial deployment. Secondly, radar signal reflections of small targets from far distance are usually weak. It is difficult to identify the weak reflections especially in the presence of environmental noise or strong reflections from other targets. The ability of IR-UWB radar in noisy environments remains unknown. Thirdly, IR-UWB radar has limited viewing angle. Our empirical studies show that a low-cost IR-UWB radar has a viewing angle of ($-60^\circ, 60^\circ$). With different materials of targets (e.g., glass wall or foam filling inside wall) in a room, the radar may fail to receive signal reflections from some targets.

Table 1. Comparison of Different Sensing Technologies and Systems for floor plan construction

	Lidar	RGB Camera	Acoustic device	mmWave radar	IR-UWB radar
Main method	Laser scan	Image analysis	Ranging	RF scan	Ranging
Floor Plan Construction System	SLAMMER [10]	Jigsaw [19]	SAMS [32]	Millimap [30]	UWBMap
Cost	High	Low	Low	High	Low
Power Consumption	High	Low	Low	Medium	Extremely low
Resistant to smoke, strong light or acoustic noise?	×	×	×	√	√
Accuracy	0.02m	< 2m	0.3m	0.2m	0.2m

In this paper, we propose UWBMap, a low-cost IR-UWB based system mounted on a mobile robot to construct floor plan through smoke. Given weak directivity and lacks of angle resolution in mono-static IR-UWB radar, instead of deploying an antenna array that will increase hardware cost and complexity, we explore motion effect by mounting IR-UWB radar on a mobile robot platform. In this way, the radar will move at a constant speed over a long-distance to form a virtual antenna array, which eventually increases angle resolution and provide spatial information of different targets. However, since floor may be uneven in real environments, the robot may experience vibration, resulting in motion noise. In this case, offsets induced by imperfect motions will be unavoidable in range measurements from received signal profile, causing distortions in target's image. Leveraging on range curve fitting over received signals, we will be able to eliminate range offset from signal profile. In addition to motion noise, environmental noise may seriously affect the process of floor plan construction. Small targets from a far distance can be easily overwhelmed by strong environmental noise. We propose to compensate energy attenuation induced by distance change, and enhance weak reflection from small objects. By setting an adaptive energy threshold, layout image can be extracted from its profile with environmental noise eliminated. Finally, due to the limitation of viewing angle of a mono-static IR-UWB radar and the restriction of its trajectory in indoor environments, we adopt multiple radars and place them in positions with complimentary viewing angles. Based on the large synthetic observation view and the combined image profiles, we design a multi-view based contour extraction and splicing method, obtaining an accurate and smooth indoor floor plan.

The main contributions of this paper can be summarized as follows.

- We use low-cost IR-UWB radars to construct floor plan. Our system has advantages of low power consumption, lightweight and easy deployment.
- We discover several key challenges of deploying low-cost IR-UWB radar in floor plan construction. We propose a virtual antenna based indoor floor plan imaging pipeline, which exploits the intrinsic radar moving characteristic to strengthen signal directivity, and eliminate noise interference from devices and environment.
- We design a multi-view based contour extraction and stitching approach, using multiple IR-UWBs, to restore complete floor plan. This method successfully overcomes the limitation of single-antenna radar with single view.
- We implement an IR-UWB based floor plan construction system mounted on a commercial mobile robot, and conduct experiments in 5 different layouts of a building. We demonstrate that the proposed system is able to construct floor plan accurately in the presence of glass wall and heavy smoke.

The rest of the paper is organized as follows. Sec. 2 presents the basics of IR-UWB sensing and the challenges of IR-UWB based indoor floor plan construction. Sec. 3 introduces the floor plan imaging algorithm, and noise elimination methods for both motion noise and environment noise. Sec. 4 introduces the multi-view based contour

extraction and splicing algorithm. Sec. 5 shows the system setup of UWBMMap and Sec. 6 reports the evaluation results. Sec. 7 discusses the limitations of our system. Sec. 8 gives a brief review of related work. Sec. 9 concludes this paper.

2 IR-UWB RADAR BASED SENSING

In this section, we first present the basis of IR-UWB radar and the properties of radar signals measured through our empirical studies. We then discuss the challenges of floor plan construction using IR-UWB radar.

2.1 Modeling IR-UWB Channel

The mono-static IR-UWB radar sends out electromagnetic impulses through the transmitting antenna periodically, which are reflected from any object in front of it. These reflections travel back via different paths, and will be received by the receiving antenna. The fundamental operations of an impulse radar system are shown in Fig. 1.

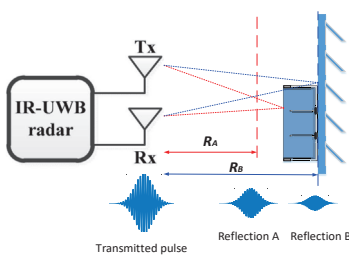


Fig. 1. The basis of IR-UWB radar.

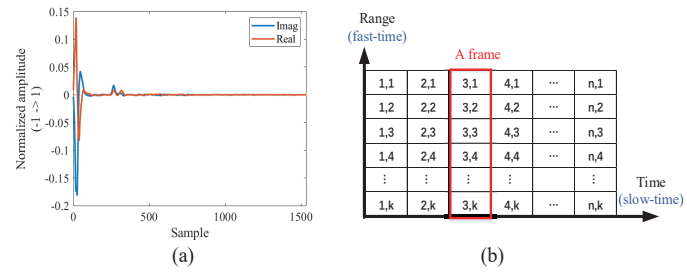


Fig. 2. Received signals sampled by IR-UWB radar. (a) A signal frame received at IR-UWB radar. (b) The received signal profile (frame matrix) [11].

The IR-UWB radar acquires the distance information R of different targets by measuring the Time-of-Flight (ToF) τ of impulses:

$$R = \frac{c \cdot \tau}{2}, \quad (1)$$

where c is the speed of light, τ is the measured time delay to the reflection, and the divisor of 2 is because the radar signal has to travel to the target and come back, hence it is twice the distance.

Take the radar we use as an example, it transmits baseband Gaussian pulse $g(t)$ with very short duration, where t is the time. After upconversion, the transmitted signal in time domain is given by:

$$s_n(t) = g(t - nT_p) \cdot \cos(2\pi f_c (t - nT_p)), \quad (2)$$

where f_c is the carrier frequency, $T_p = \frac{1}{f_p}$ is the pulse repetition interval (PRI) between two consecutive pulses, f_p is the pulse repetition frequency (the number of frames per seconds), and n denotes the number of the transmitted pulse. Note that the beam range of the transmitted signal is wide, the energy difference in different directions can be ignored. Since the impulse radio transmits a series of identical pulses, we have $\tau = t - nT_p$, where τ is the time delay of a transmitted pulse. Thus, each transmitted signal can be written as $s_n(\tau) = g(\tau) \cdot \cos(2\pi f_c \tau)$.

Considering that the signal propagates through P different paths (including direct paths and multipaths reflected by environmental objects), the impulse response of the wireless channel to the n -th pulse can be expressed as:

$$h_n(\tau) = \sum_{p=1}^P A_p \delta(\tau - \tau_p) + m(\tau), \quad (3)$$

where A_p is the channel gain of the p -th reflection path signal and is approximated as a constant, $\tau_p = \frac{2 \cdot r_p}{c}$ is the time delay of p -th path where r_p is the distance between the radar and the target, and $m(\tau)$ is Gaussian channel noise.

Therefore, the received RF signal $b_{RF}^n(\tau)$ can be obtained through the convolution operation of the transmitted signal and the channel impulse response:

$$b_{RF}^n(\tau) = h_n(\tau) * s_n(\tau) = \sum_{p=1}^P A_p \cdot g(\tau - \tau_p) \cdot \cos(2\pi f_c(\tau - \tau_p)) + m(\tau), \quad (4)$$

where symbol $*$ denotes convolutional operation.

The received baseband signal $b_n(\tau)$ after applying IQ downconversion and low-pass filtering can be obtained by:

$$b_n(\tau) = \left| b_n^{RF}(\tau) \cdot e^{j2\pi f_c(\tau)} \right|_{LPF} = \sum_{p=1}^P A_p \cdot g(\tau - \tau_p) \cdot e^{j2\pi f_c(\tau_p)} + m(\tau). \quad (5)$$

We call the received baseband signal of a transmitted impulse as a frame. As shown in Fig. 2(a), a received frame is composed of a series of complex samples. Assume the sampling rate is F_s , the fixed time interval between every two samples is $\frac{1}{F_s}$, denoting the ranging precision of a radar. The ranging precision is the error between the measured value of the target range and its true value. Noted that the sampling rate of an IR-UWB radar with a high-speed ADC module can be $23.328GS/s$, its ranging precision reaches as high as $\frac{c}{2F_s} = 6mm$ [4].

To facilitate radar signal analysis and processing, we transform the time sequence of a signal into a matrix called the received signal profile, which is an overall description of the multipath information in the environment and reflects the relationship between the distance of objects in the environment and the time.

As shown in Fig. 2(b), we arrange the reflected signals within the duration of a pulse into the same column as the *fast-time* dimension, corresponding to different time delays of distance. Radar range resolution, which also called absolute ranging accuracy, is the least radial separation between two targets in the same direction from a radar that allows them to be distinguished. The range resolution ΔR of an IR-UWB radar is directly proportional to the bandwidth B of the radar, which equals to $\frac{c}{2B}$. Assume a radar has a bandwidth of $1.4GHz$, then its range resolution is about $10cm$. IR-UWB radar always has a wide bandwidth, and can achieve high range resolution which is capable of distinguishing two objects with a small distance apart. On the other hand, while the timestamps when generating each pulse form the *slow-time* dimension, which updates every PRI, corresponding to the time sequences of the signals reflected from the same range.

The fast-time (intra-frame time/ToF) is denoted by τ and the slow-time (or inter-frame time) is denoted by t . Due to τ_p and r_p may change with time t , we have $\tau_p(t) = \frac{2r_p(t)}{c}$, the signal profile can be denoted as $b(t, \tau)$:

$$\begin{aligned} b(t, \tau) &= \sum_{p=1}^P A_p \cdot g(\tau - \tau_p(t)) \cdot \exp(j2\pi f_c \tau_p(t)) \\ &= \sum_{p=1}^P A_p \cdot g(\tau - \frac{2r_p(t)}{c}) \cdot \exp\left(j\frac{4\pi f_c r_p(t)}{c}\right). \end{aligned} \quad (6)$$

2.2 Empirical Study on IR-UWB Radar Based Floor Plan Construction

Based on our theoretical analysis, IR-UWB radar may potentially achieve high ranging resolution. We now explore the feasibility of using IR-UWB radar for floor plan construction. We first conduct our empirical study in indoor scenarios, as shown in Fig. 3. We adopt a COTS mono-static IR-UWB radar (i.e., Xethru X4M200) with



Fig. 3. Experimental setup for empirical study.

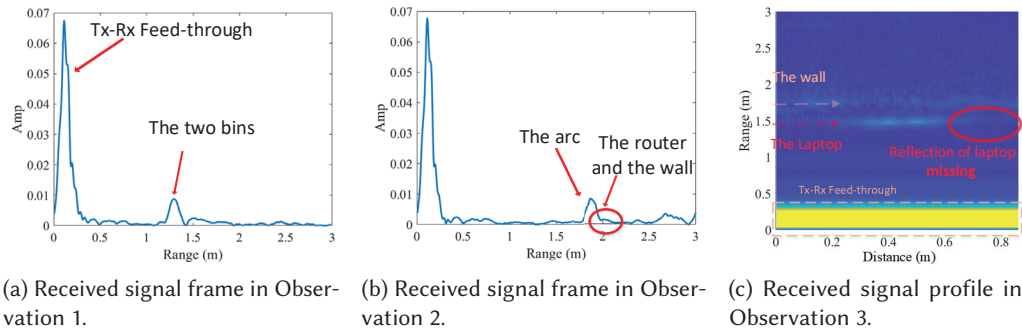


Fig. 4. Received signals in indoor environments.

7.29GHz center carrier frequency and 1.4GHz bandwidth. We record and analyze the received signals in three different scenarios, and we summarize three main observations as follows.

Observation 1: A mono-static radar lacks angle resolution to distinguish layouts of the same range but different angles.

As shown in Fig. 3a, two trash bins are placed close to the wall and separated at the same distance from the radar. The absolute value of one of the receiving frames are shown in Fig. 4a. Note that each peak of the frame corresponds to a reflector in a certain range, two bins in the same range only produce one peak, which means that a stationary mono-static radar lacks of angle resolution to distinguish objects at different angles, and it also lacks the ability to distinguish layout information in different directions.

Observation 2: The reflections of small targets with low power are difficult to identify and may be overwhelmed by the strong reflectors or environmental noise.

To explore whether small targets can be identified under strong interference, as shown in Fig. 3b, we hang a WiFi router on the wall and place a large cardboard next to it. The reflection area of the router is small, the cardboard has a semicircular shape with tin foil inside, resulting in strong reflections at almost every angle in the front. Fig. 4b shows the received frame and demonstrates that the reflected energy of the router is particularly weak under the influence of the strong reflection of the cardboard. In addition to the original reflections from the two targets, the radar also suffers from strong device noise induced by Tx-Rx leakage, appearing as a strong pulse starting at the first fast-time number. Besides, the interference of multipath reflections also occur, showing the same energy level as the router's reflection. Therefore, it is difficult to identify low-energy reflectors in floor plan construction.

Observation 3: A mono-static radar may only receive reflections from partial targets of the layout, inducing limited observation view for the whole floor plan environments.

To explore the difference of received signals collected at different spatial positions, we adopt a metal casing laptop near the wall and change the locations of the radar uniformly in a straight line from left to right with 5mm

distance intervals, as shown in Fig. 3c. While the radar can receive the weak reflections from the wall at almost all the time, as can be seen in Fig. 4c, the reflection of the laptop increases first and then decreases, reaching the maximum when the beam center reaches the target center. The reflection of laptop is missing when the radar locates at the beginning part and end part. Hence, when the spatial position of radar is restricted and fixed, the radar may only receive reflections from partial targets, resulting limited observation view. It's hard to obtain a complete floor plan of all targets of the layout.

The above observations imply three main challenges when applying IR-UWB based to floor plan construction, i.e., lack of angle resolution, difficulty in identifying objects with weak energy in noise interference, and limited observation view. We aim to address these challenges in the design of UWBMap in the following sections.

3 FLOOR PLAN IMAGING USING A MOVING IR-UWB RADAR

In this section, we model our virtual antenna array via a moving radar to capture spatial information, and present our imaging method to construct floor plan effectively. The imaging algorithm acquires both range and angle resolution, however noise interference may still weaken image quality. Since noises from device and environment may cause distortion in the imaging process and affect the extraction of effective floor plan information, we propose the corresponding noise elimination methods, including motion noise cancellation and environmental noise migration.

3.1 Modeling Radar Moving Process for Floor Plan Construction

Synthetic Aperture Radar (SAR) has been widely used in radio frequency imaging for remote sensing applications, such as earth observation and military surveillance [13]. Its basic idea is to move a radar with small aperture over a long distance to compose a virtue antenna array to emulate a large-aperture radar [31]. This helps to generate images (the spatial positions) with much higher angle resolution. During the movement, the standard SAR radar usually sends linear frequency modulation (LFM) signals periodically and collects the reflected signals from several kilometers away to generate images. Similar to remote sensing, the task of floor plan construction is to acquire a 2-D image of an indoor layout.

Note that a mono-static IR-UWB radar constantly moves along a straight line. It periodically receives signal reflections from indoor layouts with uniform space position and obtains the distance between the radar and the reflecting point by analyzing the signal frames. Therefore, as shown in Fig. 5a, the model of floor plan imaging includes three axes named range r , distance x and depth y .

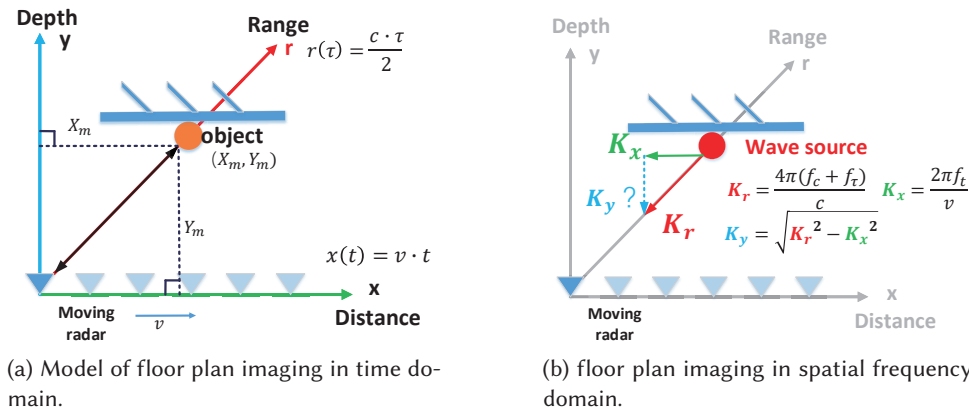
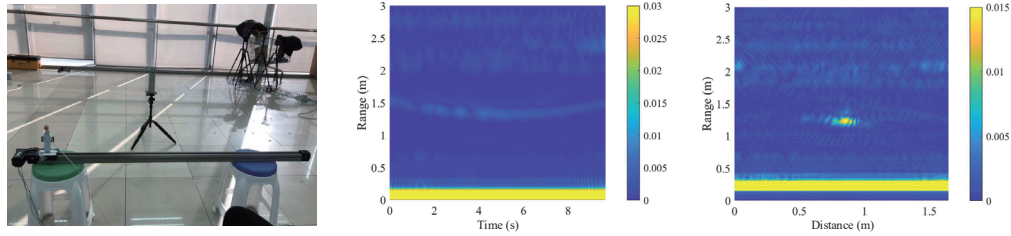


Fig. 5. Models of radar moving to form virtual antennas.



(a) A stainless steel cup as a point target. (b) The signal profile of the cup. (c) The image profile of the cup after processing by ωKA .

Fig. 6. Experiments with single target.

The range axis r is denoted by fast-time number τ as mentioned in Sec. 2.1. Since fast-time number τ means the time delay of certain range, the range difference between two adjacent fast-time samples within a frame is $\frac{c}{2F_s}$, where F_s denotes the sampling rate. The range resolution Δr of the radar is $\frac{c}{2B}$. The distance axis x with slow-time number t shows the movement distance and the spatial sampling position of the radar (the horizontal coordinates). To avoid the aliasing effect, the imaging requires the cross-range spacing between consecutive pulse sampling locations to be within $\frac{\lambda}{4}$, where λ denotes the signal wavelength [35]. The resolution in distance axis, which also called azimuth resolution, shows the ability of radar equipment to separate two targets at similar ranges but different bearings from a reference point. It depends on the length of the synthetic aperture. When imaging targets are always in the field-of-view of the radar, the longer the distance of azimuthal motion we have, the higher the resolution we achieve. However, when the targets are not covered by the radar, the resolution is only decided by the antenna size. The depth axis y demonstrates the vertical coordinates of different targets.

As shown in Fig. 5, we assume the radar moves from the origin of the coordinate axis ($x = 0, y = 0$) along the distance axis at a constant speed v , and the range values r is recorded across time. The horizontal coordinates can be calculated by $x = v \cdot t$. A target (such as a round pillar) is placed at (X_m, Y_m) of x - y coordinates, where Y_m denotes both the depth value and the minimum distance between the target and the radar while moving.

The range value between pillar and radar over time t has the following relations:

$$r(t) = \sqrt{Y_m^2 + (x - X_m)^2} = \sqrt{Y_m^2 + (vt - X_m)^2} = Y_m \sqrt{1 + \left(\frac{vt - X_m}{Y_m}\right)^2}. \quad (7)$$

As shown in Fig. 6a, if we drive the radar using a high precision programmable linear motion slider (1.5m long) at a constant speed and place a stainless steel cup at a position 1.25m facing the center of the slide rail, the received signal profile (Fig. 6b) appears a decrease and increase pattern.

Considering that a floor plan image are essentially the coordinates of the horizontal and vertical axes, the **key idea** of floor plan imaging is to convert the *distance – range* signal profile to the *distance – depth* image profile.

3.2 Floor Plan Imaging

To accurately and efficiently obtain the target position on the depth axis, we use ωK Algorithm (ωKA), which is suitable for large aperture radar and near field imaging [13]. ωKA conducts the SAR imaging in spatial frequency domain, and acquires the depth information of the target by wave vector decomposition.

Different from *frequency* (traditional temporal frequency) which refers to the number of occurrences of a repeating event per unit of time and is measured in hertz (Hz), *spatial frequency* is a characteristic of any structure that is periodic across position in space [7]. The wave vector \vec{K} is the spatial frequency of a wave. Its direction denotes the propagation of a wave and its magnitude is measured in radians per unit distance, which can be denoted by $|\vec{K}| = \frac{2\pi}{\lambda} = \frac{2\pi f}{c}$, where λ is the wavelength, f denotes frequency and c denotes speed of the wave.

The floor plan imaging model in spatial frequency domain is shown in Fig. 5b. In spatial frequency domain, the static target is regarded as a wave source. It periodically transmits waves with twice the frequency to the radar receiver along the (reverse) range axis. The magnitude of the wave vector \vec{K} is K_r . Due to the position of the radar keeps changing, the propagation direction of the wave to the radar also changes. Hence, the magnitudes of the wave projected on the x -axis and y -axis, which are K_x and K_y , change accordingly. Due to the distance between two adjacent sampling point of the radar is very small, the transmitting wave can be seen as a plane wave. Therefore, the wave vector can be decomposed based on the following equation: $K_r^2 = K_x^2 + K_y^2$. Since $x = v \cdot t$ and $r = \frac{c \cdot \tau}{2}$, the received signal profile $b(t, \tau)$ in Eq. 6 can transformed to $K_x - K_r$ spatial frequency profile by performing 2D Fast Fourier Transform (FFT), where $K_x = \frac{2\pi f_t}{v}$ and $K_r = \frac{4\pi(f_c + f_\tau)}{c}$. It is worth noting that since the signal propagation distance is twice the distance between the radar and the target, the spatial frequency K_r is equal to twice the product of the transmit frequency $f_c + f_\tau$ and $\frac{2\pi}{c}$. Hence, we can substitute K_r with variable K_y and obtain the $K_x - K_y$ profile. After performing 2D IFFT on $K_x - K_y$ profiles, we eventually get the desired $x - y$ imaging profile with distance and depth coordinates of the target.

More specifically, we describe the steps of ωKA as follows.

First, we apply 2D FFT to transform the received signal profile $b(t, \tau)$ from time domain to 2D frequency domain $B(f_t, f_\tau)$. The 2D-FFT can be transformed into two 1D-FFT, so we first consider τ and then t . The parameter τ is only included in a Gaussian function, and the result of its Fourier transform can be directly written as another Gaussian function¹. The other parameter t is more complicated, so we get the approximation of Fourier transform result based on the Principle of Stationary Phase (POSP) [35]. Finally, $B(f_t, f_\tau)$ can be expressed as:

$$B(f_t, f_\tau) = \text{FFT}_{t, \tau}[b(t, \tau)] = \sum_{p=1}^P A'_p \cdot G(f_\tau) \cdot \exp\left(j \frac{2\pi f_t X_m}{v} + j \frac{4\pi Y_m}{c} \sqrt{(f_c + f_\tau)^2 - \frac{c^2 f_t^2}{4v^2}}\right), \quad (8)$$

where A'_p is a constant number and $G(f_\tau)$ is a Gaussian function. f_t and f_τ denotes the frequency of distance change of radar across distance axis and the frequency of distance change between the radar and the target.

Second, we transform the frequency profile $B(f_t, f_\tau)$ to the 2D spatial frequency domain $B(K_x, K_r)$. Let $K_x = \frac{2\pi f_t}{v}$ and $K_r = \frac{4\pi(f_c + f_\tau)}{c}$, the $f_t - f_\tau$ frequency domain can be transformed to $K_x - K_r$ spatial frequency domain, and equation 8 can be expressed as:

$$B(K_x, K_r) = \sum_{p=1}^P A'_p \cdot G'(K_r - \frac{4\pi f_c}{c}) \cdot \exp\left(j \cdot X_m \cdot K_x + j \cdot Y_m \cdot \sqrt{K_r^2 - K_x^2}\right). \quad (9)$$

K_r and K_x denotes the magnitude of wave along different r -axis and x -axis direction, which also equals to the phase changes speed per meter across range axis and distance axis. They are related to the speed of light c and the moving speed v of the radar respectively.

Third, we transform $B(K_x, K_r)$ to $B(K_x, K_y)$ by performing variable substitution from K_r to K_x in spatial frequency domain based on equation $K_r^2 = K_x^2 + K_y^2$. Substituting $\sqrt{K_r^2 - K_x^2}$ with K_y , Eq. 9 can be re-expressed as:

$$B(K_x, K_y) = \sum_{p=1}^P A'_p \cdot G'\left(K_r - \frac{4\pi f_c}{c}\right) \cdot \exp\left(j \cdot X_m \cdot K_x + j \cdot R_m \cdot K_y\right), \quad (10)$$

¹Considering a Gaussian function $g(\tau - \mu) = \frac{1}{\sqrt{2\pi}\sigma} \cdot \exp\left(-\frac{(\tau-\mu)^2}{2\sigma^2}\right)$, its frequency profile after performing FFT over τ can be expressed as: $\frac{1}{\sqrt{2\pi}} \cdot \exp\left(-\frac{\sigma^2\omega^2}{2}\right) \cdot \exp(j\omega\mu) = \frac{1}{\sigma} \cdot G(\omega) \cdot \exp(j\omega\mu)$, where $\omega = 2\pi f_\tau$.

showing the relationship between K_x and K_y . This variable substitution completes the mapping from range to depth and changes the phase of the distance domain and range domain at the same time. Technically, we use Stolt interpolation to get uniformly sampled signals.

In the final step of the method, we perform 2D-IFFT on $B(K_x, K_y)$, and obtain a desired floor plan image $b(x, y)$. Fig. 6c shows the resulting image profile of a cup. After processing by ωKA , it is transformed from *distance – range* signal profile (Fig. 6b) to the *distance – depth* image profile.

3.3 Motion Noise Cancellation

Theoretically, the radar moves in a straight line with a constant speed, and obtains signal frames in uniform positions on the line. After processing by the imaging algorithm, the raw received signal profile can be transformed into a floor plan image, demonstrating the accurate spatial positions of the indoor layout.

However, in practice, the ground of a floor may not be always flat and even, making the robot unable to collect signals smoothly and uniformly along the line. Therefore, a deviation of range between target and radar may rise, leading to a distorted signal profile and an unfocused floor plan image.

When the robot equipped with an IR-UWB radar moves in the scenario shown in Fig. 3b, the collected received signal profile is shown in Fig. 7a. In the raw signal profile, we can see a straight and a quadratic curve correspond to the wall (with the router) and the arc. Fig. 7c shows the image profile after floor plan imaging. Compared with the ground truth of imaging (the orange dash lines) in Fig. 7b, some parts of the image in Fig. 7c are out of focus. We can see that the image of the router is missing, and the image of the arc is incomplete. Note that there exists strong interference of the antenna energy leakage, we eliminate the Tx-Rx feed-through first. Concerning that for a certain equipment, the corresponding feed-through is relatively fixed as time changes. So, we measure this device noise in advance in an open environment, and then subtract this tested value from each collected receiving signal frame when using.

Considering the range deviation (offset) between the ideal sampling position and that of the actual one, we apply a motion noise cancellation before the step of floor plan imaging, intending to eliminate the distance measurement errors. We noticed that the theoretical range change of between the radar and a static target $r(t)$ (Eq. 7) is quite similar to a quadratic function especially when $|\frac{gt-X_m}{Y_m}| \leq 1$. This indicates that when the angle between the target and the radar beam center belongs to $[-45^\circ, 45^\circ]$, the range change $r(t)$ can be fitted well as a quadratic function. This assumption holds true because the viewing angle of IR-UWB radar is limited and the beam energy attenuates from the center to the surroundings. Therefore, we approximate $r(t)$ as a quadratic function $ax^2 + bx + c$, where $a \geq 0$ and $c > 0$. Since the received signal is the superposition of multipaths' signals, the sum of all the targets' range $\sum_{p=1}^P r_p$ also follows a quadratic function.² The **core idea** of motion noise cancellation is to extract the sum of all targets' range changes from the received signal profile, use an ideal quadratic curve to correct the range offset induced by imperfect robot motion, and further eliminate the range offset from the signal profile.

Extracting the target's range change is the first key step of motion noise cancellation, which relies on cleverly constructing mathematical formulas. The main intuition is to eliminate the interference of the amplitude term and extract the range change from the phase term of the received signal through the derivative operation.

Assume that the range offsets across time is $\Delta(t)$, then the actual distance between the radar and a target is $r(t) + \Delta(t)$, and the actually received signal profile $m(t, \tau)$ can be denoted by:

$$m(t, \tau) = \sum_{p=1}^P A_p \cdot g(\tau - 2\frac{r_p(t) + \Delta(t)}{c}) \cdot \exp\left(j4\pi f_c \frac{(r_p(t) + \Delta(t))}{c}\right), \quad (11)$$

² $\sum_{p=1}^P (a_p x^2 + b_p x + c_p) = (\sum_{p=1}^P a_p)x^2 + (\sum_{p=1}^P b_p)x + (\sum_{p=1}^P c_p) = Ax^2 + Bx + C$.

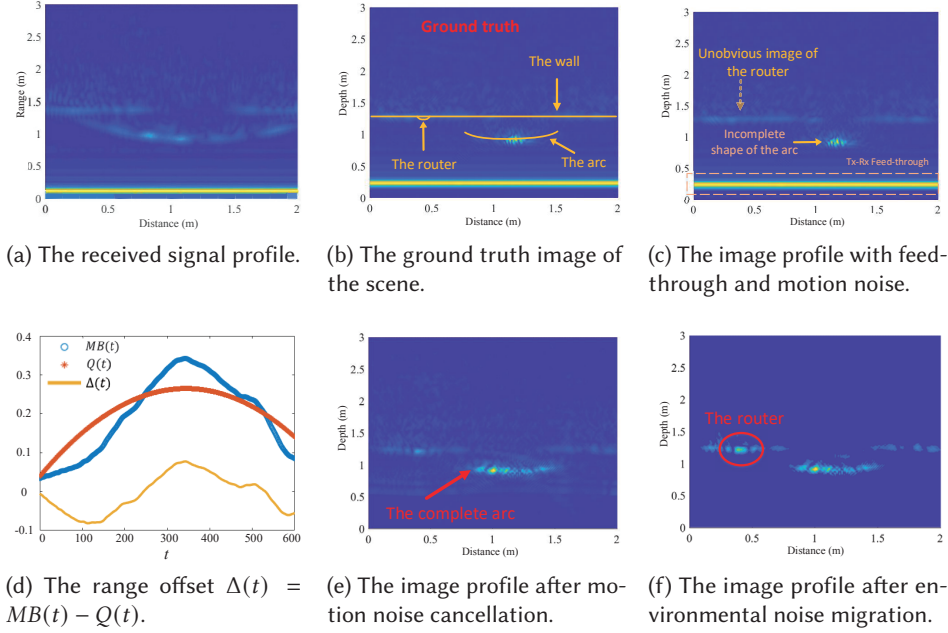


Fig. 7. The experiment of an arc and a router near the wall.

where p denotes the number of different reflect paths (targets). We can see that the range change $r_p(t) + \Delta(t)$ appears both in the Gaussian term and phase term of the signal profile. Compared with extracting range change directly from the Gaussian term, if we can transform the Gaussian to a constant, it's easier to extract it from the phase term by performing the partial derivative with respect to time.

So, we apply 1D-FFT on each column of the input signal profile over range axis. Same as Eq. 8, since the Fourier transformation of $g\left(\tau - 2\frac{r_p(t) + \Delta(t)}{c}\right)$ equals a constant number multiply $G(f_\tau) \cdot \exp\left(j4\pi f_\tau \frac{r_p(t) + \Delta(t)}{c}\right)$, the frequency spectrum $M(t, f_\tau)$ is denoted by:

$$M(t, f_\tau) = \text{FFT}_\tau(m(t, \tau)) = \sum_{p=1}^P A'_p \cdot G(f_\tau) \cdot \exp\left(j\frac{4\pi(f_c + f_\tau)}{c}(r_p(t) + \Delta(t))\right), \quad (12)$$

where A'_p is a constant number and $G(f_\tau)$ is a Gaussian function. Since IR-UWB radars have wide bandwidth, which means f_τ is wide, so we can approximate $G(f_\tau)$ as a constant and omit it.

Then, let $K_r = 4\pi(f_c + f_\tau)/c$, we transformed $M(t, f_\tau)$ to the spatial frequency spectrum $M(t, K_r)$, which can be expressed as:

$$M(t, K_r) \approx \sum_{p=1}^P A'_p \cdot \exp(jK_r(r_p(t) + \Delta(t))). \quad (13)$$

To extract $r_p(t) + \Delta(t)$ from the phase term of Eq. 13, we perform the partial derivative of $M(t, K_r)$ with respect to t , which can be expressed as:

$$\tilde{M}(t, K_r) = \frac{\partial M}{\partial t} = \sum_{p=1}^P jA'_p K_r (r_p(t) + \tilde{\Delta}(t)) \cdot \exp(jK_r(r_p(t) + \Delta(t))), \quad (14)$$

where (\cdot) denotes the derivative with respect to t . We can see that the derivative of range change $(\tilde{r}_p(t) + \tilde{\Delta}(t))$ becomes a factor. And we need to keep the factor and further eliminate other factors. So we construct the following equation:

$$\begin{aligned} mB(t) &= \frac{Im(\sum_{K_r} \tilde{M}(t, K_r) \cdot M^*(t, K_r) / K_r)}{\sum_{K_r} M(t, K_r) \cdot M^*(t, K_r)} \\ &= \frac{Im(j \sum_{p,q=1}^P A'_p A_q^* (\tilde{r}_p(t) + \tilde{\Delta}(t)) \sum_{K_r} \exp(j K_r (r_p(t) - r_q(t))))}{\sum_{p,q=1}^P A'_p A_q^* \sum_{K_r} \exp(j K_r (r_p(t) - r_q(t)))}, \end{aligned} \quad (15)$$

where $Im(\cdot)$ denotes the imaginary part of a complex number, p and q denote the number of paths correspond to targets, $(\cdot)^*$ denotes the complex conjugate. In Eq. 15, the factor K_r is deleted by division, and the phase term $\exp(j K_r (r_p(t) + \Delta(t)))$ will be eliminated by multiplying by $M^*(t, K_r)$, as well as the A'_p by divided by $M(t, K_r) \cdot M^*(t, K_r)$.

Since it is reasonable to assume that the difference between r_p and r_q is larger than the wavelength of the IR-UWB signals, we have $\sum_{K_r} \exp(j K_r (r_p(t) - r_q(t))) \approx Z \delta_{pq}$, where Z is a constant. If $p = q$, then $\delta_{pq} = 1$ otherwise $\delta_{pq} = 0$. Only the same paths ($p = q$) are retained in the Eq. 15 while different paths will cancel each others out. Therefore, we can approximate $mB(t)$ as:

$$mB(t) \approx \frac{\sum_{p=1}^P |A'_p|^2 (\tilde{r}_p(t) + \tilde{\Delta}(t))}{\sum_{p=1}^P |A'_p|^2} = \sum_{p=1}^P \frac{|A'_p|^2}{\sum_{q=1}^P |A'_q|^2} \tilde{r}_p(t) + \tilde{\Delta}(t) \quad (16)$$

To get the value of $\Delta(t)$, we then integrate $mB(t)$ with respect to t , the result can be denoted by:

$$MB(t) = \int_t mB(t) dt = \sum_{p=1}^P \frac{|A'_p|^2}{\sum_{q=1}^P |A'_q|^2} r_p(t) + \Delta(t) \quad (17)$$

The first part of the equation should follow a quadratic pattern as the $r_p(t)$ is a quadratic curve.

As shown in Fig. 7d, we finally fit the above equation $MB(t)$ with a quadratic curve $Q(t)$. Thus, the range offset $\Delta(t) = MB(t) - Q(t)$. We can substitute it into Eq. 11 to correct the distorted range changes of signal profile. Fig. 7e shows the image profile after motion noise cancellation and floor plan imaging. We can observe the correct and complete image of the arc.

3.4 Environmental Noise Migration

In addition to motion noise, noise from the environment may seriously affect the process of floor plan construction. In this section, we propose an environmental noise migration method to effectively eliminate environmental noise. This method also adaptively extracts valuable information from the image of a floor plan. The methods consists of two main steps, including depth-based energy compensation and adaptive floor plan extraction from noisy environment.

3.4.1 Depth-based Energy Compensation. After mapping the received signal profiles to the floor plan image, we obtain both the range and depth information of the layout. While the spatial positions are obtained accurately, the energy of the targets in the floor plan image is still distorted without considering the energy attenuation caused by the increase in distance. Therefore, we conduct the depth-based energy compensation on floor plan images by multiplying a scale factor to the depth axis. The scale factor can be denoted by:

$$scale(y) = \min(thre, 1 + (\frac{3y}{max})^4), \quad (18)$$

where y denotes depth of a target in the floor plan image, \max denotes the maximum value of depth and $thre$ is a preset threshold. Considering that the target usually appears at a relatively close distance, we could even remove the depth values greater than the threshold in the image profile, thereby eliminating the influence of multipath interference (such as multiple reflections).

The energy compensation for different targets is gradually increased from near to far. When the depth of the target exceeds a certain value, the scale factor will be fixed at threshold $thre$. After this compensation step, the impact of noise from small depth is weakened and the energy of targets with big depth is enhanced. In this way, both floor plan information from every depth can be better recognized and extracted.

3.4.2 Adaptive Floor Plan Extraction in Noisy Environment. Note that images after energy attenuation compensation may still contain noise interference, such as multipath noise and white Gaussian noise. In addition, there also exist unfocused imaging noise in the image profile such as the sidelobes of targets' image. The sidelobes produced by targets with strong reflection may obscure objects with weak reflection. Moreover, the position where the sidelobes intersect will produce "ghost targets", leading to erroneous contour information extraction. Hence, the purpose of adaptive floor plan extraction is to eliminate both the above noise interference as much as possible, generating a clean image containing only the objective floor plan components.

Based on the assumption that the image points of the real targets in the image profile must have the strongest reflection power, the **main steps** of the algorithm are as follows. First, we select a fixed percentage of energy values in the input image profile as the adaptive threshold to remove low power multipath noise and white Gaussian noise. Since the threshold is not an absolute value, it changes with different inputs and has good adaptability. Second, we iteratively extract several points with the strongest energy from the time-domain image profile, remove these points themselves and their sidelobes in the spatial frequency domain, until all points in the image profile above the adaptive threshold have been processed. Since the number of target points is limited in the indoor environment, we can extract objective image points of all targets through fewer iterations.

Note that sidelobe elimination is one of the key points for floor plan construction. We first figure out the source of the sidelobe interference and propose the corresponding elimination method.

We find that the sidelobes are induced by the incompleteness of valid the 2D spatial frequency domain of the image profile after floor plan imaging. The smaller the valid frequency domain is, the larger the sidelobes of the time domain image profile are induced. Two reasons may lead to the incomplete spatial frequency spectrum. On the one hand, the radar has limited beamwidth, which only receives target reflections within a certain angle range. As mentioned in Sec. 3.2, $K_r = \frac{4\pi(f_c + f_t)}{c}$ denotes the magnitude of the signal wave in the spatial frequency of a wave and can be projected on the x -axis and y -axis, which are K_x and K_y in Fig. 5b. If the angle of the radar to the target is θ and the maximum beamwidth is θ_{max} , then $K_x = K_r \sin \theta$, $K_y = K_r \cos \theta$, and the frequency spectrum where $\frac{K_x}{K_y} > \tan \theta_{max}$ is missing (set to 0). On the other hand, the radar has limited ADC sampling rate, which restricts the maximum value K_{rmax} of K_r . When we transform transform $B(K_x, K_r)$ to $B(K_x, K_y)$ (Eq. 9 to Eq. 10) by performing variable substitution from K_r to K_x in spatial frequency domain based on $K_r^2 = K_x^2 + K_y^2$. Therefore, the spatial frequency spectrum where $K_x > \sqrt{K_{rmax}^2 - K_y^2}$ cannot be obtained by interpolation. Hence, the range of sidelobe interference are $\frac{K_x}{K_y} > \tan \theta_{max}$ and $k_x > \sqrt{K_{rmax}^2 - K_y^2}$.

The sidelobe cancellation is conducted in the 2D spatial frequency domain. We first perform 2D-FFT to the image points selected from the image profile during iteration. Then, we set the same absence as the whole spatial frequency domain to the result of 2D-FFT, which causes the selected points to produce a sidelobe. Finally, we subtract the simulated sidelobe from the whole image profile in the 2D spatial frequency domain to acquire the cleaned data. More specifically, the process of sidelobe cancellation can be denoted by: $fftData - 2FFT(sData) \cdot mask$, where $fftData$, $sData$, and $mask$ denotes the 2D spatial frequency profile of the image profile, the image

Algorithm 1 The layered floor plan extraction algorithm

Input: $data = b(x, y)$; $valThre = \text{prctile}(w, data)$; $mask$;
Output: cleanedData

```

1:  $fftData = 2FFT(data)$ ;  $\text{cleanedData} = \text{zeros}(\text{size}(data))$ 
2: for  $iter = 1 : maxIter$  do
3:    $data = 2IFFT(fftData)$ 
4:   % Find the coordinates of the first  $countPerIter$  elements in  $\text{abs}(data)$  with a value greater than  $valThre$ 
5:    $idx = \text{FindTopK}(\text{abs}(data), valThre, countPerIter)$ 
6:   if  $\text{size}(idx) == 0$  then
7:     break
8:   end if
9:    $\text{cleanedData}(idx) = \text{cleanedData}(idx) + data(idx)$ 
10:   $dataNew = \text{zeros}(\text{size}(data))$ ;  $dataNew(idx) = data(idx)$ 
11:   $fftData = fftData - 2FFT(dataNew) \cdot mask$ 
12: end for

```

profile of selected points, and the range of sidelobes in the 2D spatial frequency. $2FFT$ and $2IFFT$ denotes the 2D-FFT and 2D-IFFT, respectively.

The complete algorithm is illustrated in Alg. 1. The input data is the image profile after energy compensation, the adaptive threshold which is a fixed percentage w of energy values, and the calculated sidelobe range $mask$. Instead of processing all selected image points at once, we process these in batches that are composed of a fixed number of image points $countPerIter$ through different iterations. The output of the algorithm is a clean image profile with only the effective floor plan information.

Referred to the setting in Observation 2 (Sec. 2.2), a router is attached on a concrete wall shown in Fig. 3b. Fig. 7a and Fig. 7e show the raw signal profile and the image profile before adaptive noise elimination. Due to the small reflection cross section, the router corresponds to only a small amount of points with pretty low energy in the image profile, which can be difficult to recognize and extract. With the proposed adaptive noise elimination method, as shown in Fig. 7f, we successfully extract the clear image of the router, eliminating environmental noise.

4 MULTI-VIEW BASED FLOOR PLAN CONTOUR EXTRACTION

In this section, we first demonstrate the challenge of using a single mono-static IR-UWB radar with limited viewing angle for floor plan construction. We then introduce a multi-view based contour extraction and splicing algorithm to achieve complete floor plans.

4.1 Limited Observation View of a Single Radar

Although the uniform linear motion give the mono-static radar spatial resolution, leading to a floor plan image after processed by SAR imaging algorithm. It is still uncertain whether a single moving radar equipped on a mobile platform is enough for high quality floor plan construction.

Here, as shown in Fig. 8, we conduct an experiment to present this problem and explore the relationship between radar viewing angle and the floor plan image. We deploy 3 mono-static IR-UWB radars with different viewing angles (shown in Fig. 8b) on one side of a robot platform facing the wall. The robot are controlled to move in constant speed of $0.3m/s$ from left to the right parallel to the wall. Assume the moving direction is 180° , then the viewing angle of three radars facing left side, front, and right side are 30° , 90° and 150° . A paper arc

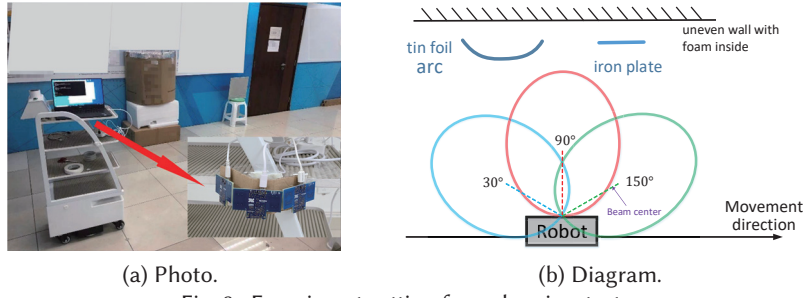


Fig. 8. Experiment setting for radar view test.

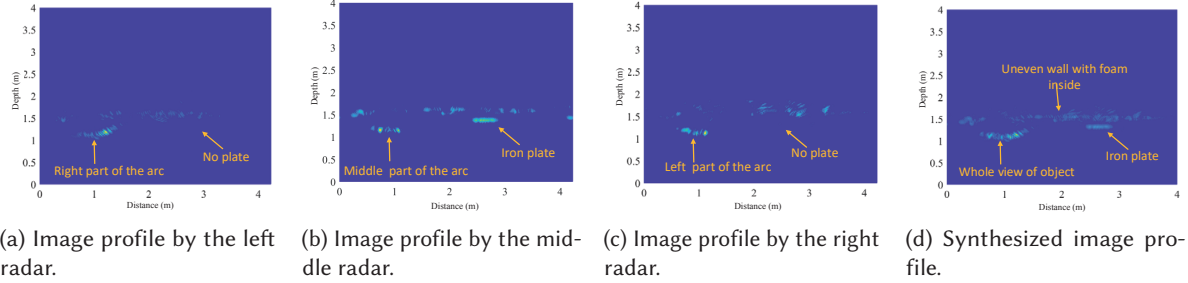


Fig. 9. Multiple radars for floor plan construction.

with tin foil inside and an iron plate are placed near the wall. The wall is non-solid, with a layer of foam board attached to the surface, and the foam board is uneven underneath.

Under the condition of restricted trajectory, Fig. 9a, 9b and 9c shows the extract image profiles of the three radar devices. We find that a single radar has fixed viewing angle and can only receive reflections from partial layouts. The reasons behind come from two aspects:

1) The low-cost IR-UWB radars have directional antenna and have the limited viewing angle of $(-60^\circ, 60^\circ)$. The left radar, middle radar and right radar can only acquire the right, middle and left part of the arc. The beam energy attenuates from the center to the surroundings. Hence, some targets are not covered by beams with stronger energy and can not be observed in signal profiles obviously. Fig. 9d shows the image profile after summing the profiles of the three devices. It is worth note that, these radars with different viewing angles may complement each other, which is equivalent to a more powerful radar with a large viewing angle.

2) Different targets with different materials have corresponding reflection coefficients and patterns. As shown in Fig. 9, the iron plate can only be seen in the image profile of the middle radar, while other two radars cannot. This is because the surface of the iron plate is smooth, the reflection coefficient is high. Thus, when the incident angle of the radar is large with respect to the smooth surface, most of the incident signals are specularly reflected into the environment (gradually attenuated and disappeared or becomes multiple reflection interference) and may not even be received by the Radar. Hence, even if the target is within the radar's beam coverage, it still cannot be observed. In addition, we also observe that the continuity varies from different parts of images which correspond to the wall, the arc and the plate. The reflection patterns vary from different materials. As shown in Fig. 10a, when the target is an object with a smooth surface (such as the iron plate), specular reflection occurs. The radar can receive the reflections when the beam is perpendicular to the surface of the object. Therefore, the change of the target image is continuous, and the reflection signal is the strongest when it is vertical. For targets with rough surfaces (such as the wall with foam inside), as shown in Fig. 10b, the radar beam scatters in all directions with different energy. So images of these targets is uneven and discontinuous.

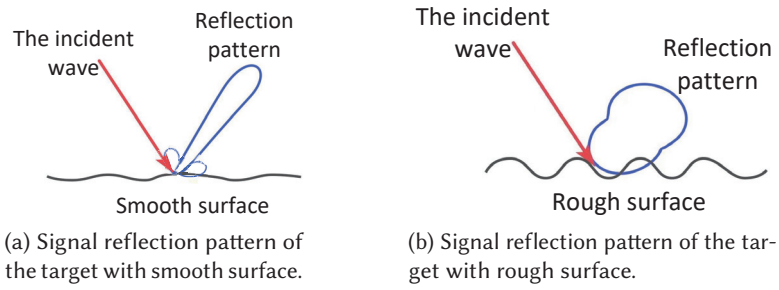


Fig. 10. Reflections of different targets with rough or smooth surface.

In summary, a single radar has the limited observation view. Multiple radars with different observation angles may complement each other, inducing a larger synthetic observation view. The larger angle of the radar heading, the wider the effective observation area, which is more conducive to the observation and imaging of the whole floor plan. Besides, the image of a target may appear discontinuous and partially missing, making it more difficult to extract accurate contour lines from the image profiles.

4.2 Multi-view Based Contour Extraction and Splicing

Next, we introduce how to extract contour lines from the synthetic image profile collected by multiple radars with different observation views and how these contour lines of different trajectory make up a complete floor plan.

4.2.1 Principle of Multi-view Based Floor Plan Construction. Based on the above experiment and analysis, due to the limited observation view of a radar with directional antenna, the radar is required to move through different path to provide sufficient observation views for accurate floor plan construction. However, under adverse environmental conditions, it is vital to obtain floor plans as quickly as possible for rescue while the moving trajectory of the radar is often limited. Therefore, to ensure a wider observation viewing angle for identifying targets from different angles as much as possible, adding more radar devices with complementary viewing angles is a feasible and effective solution.

The principle of multi-view based floor plan construction is described as follows. Ensure that at least one radar receive strong back reflection from the layout at each spatial sampling position during the movement. So that regardless of the material of the object or the angle of the reflection of the target, the radar always obtains the reflected signal with sufficient energy to form a clear floor plan image. Note that greater angle difference between the beam center of different radars implies stronger complementarity. However, if the angle difference is too large, the beam energy attenuation will result in a decrease in the imaging performance. Therefore, it is important to balance complementarity and imaging performance.

We require the synthetic observation viewing angle of one trajectory $\theta_{syn} > 180^\circ$. Since the energy of the transmitted signal reaches its maximum at the beam center, we require one-half of the angle in the middle of the beam of multiple devices to cover the sensing range:

$$z \cdot \frac{1}{2} \cdot \theta > \theta_{syn} \quad (19)$$

where z is the number of radar, θ is the field-of-view in distance axis, θ_{syn} is the angle of synthetic observation view.

Since the azimuthal field-of-view of IR-UWB radar from our empirical study is about 120° where $\theta \in [-60^\circ, 60^\circ]$, to ensure the quality of floor plan construction, we deploy 3 radars in our system. Each radar has a different viewing angle, our system is basically a multi-view based floor plan construction system.

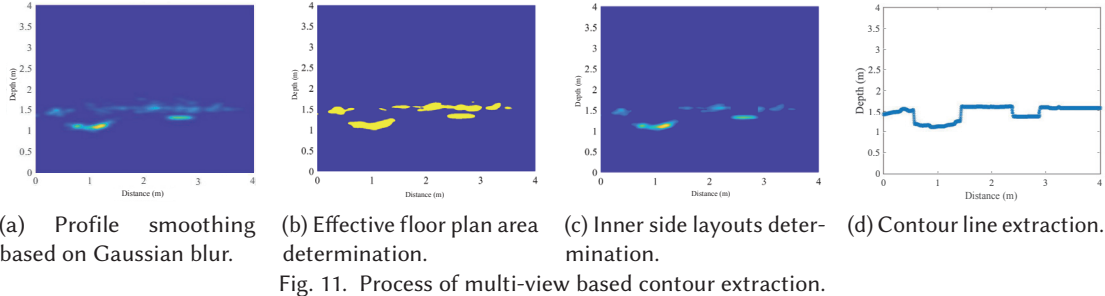


Fig. 11. Process of multi-view based contour extraction.

4.2.2 Multi-view Based Contour Extraction. We sum all the extracted image profiles of multi-view radars by time and obtain synthetic image profiles as the input of our contour extraction method. As shown in Fig. 9d, the synthetic profile contains almost complete contours of the wall, the iron plate and the arc.

The multi-view based contour extraction algorithm operates in the following steps:

- **Profile smoothing based on Gaussian blur.** Due to the difference in reflection coefficients of different materials, the continuity and smoothness of an image containing different objects will be different in the synthetic profile. Object occlusion can also cause discontinuous contours. Thus, we leverage Gaussian blurring on the image to make the contour continuous and smooth, as shown in Fig. 11a. However, choosing the right Gaussian kernel is critical. It should be noted that a large Gaussian kernel will over-smooth and lose details of the contour, but a small Gaussian kernel will not achieve the effect of filling and smoothing. We use a relative small kernel on the depth to ensure the accuracy of depth value of the contour line and a relative big kernel on the distance axis for smoothing.
- **Effective floor plan area determination.** After performing image blurring, we extract image points whose energy is higher than a certain threshold to further eliminate the residual noise (Fig. 11b). The threshold is determined by picking the energy value with a fixed percentage of all points in the profile, which has good adaptability for different inputs. Since a floor plan shows the contour lines for inner side layout, we partition the image points of each distance coordinate and keep the points in the nearest area, as shown in Fig. 11c. The target's image is divided into few segments. It's worth noted that all wall segments of the layout may not be joined directly, such as the door of a room is open and the corridor is semi-enclosed. If the depth change of adjacent segments in the image profile is greater than a certain threshold (such as 1.5m), we consider that the distant segment does not belong to the floor plan of the current room. In addition, if the distance coordinate change between two adjacent segments is greater than a certain threshold, we consider that no target exists at the segment interval, so no contour extraction is performed in the interval.
- **Contour line extraction.** We extract the series of points with max energy of each column in the image profile as the contour line and interpolate the missing points in the middle of the line. We further filter the line to eliminate outliers and obtain a smoother result. Fig. 11d shows the result of contour line extraction, which is pretty close to the ground truth value.

4.2.3 Contour Splicing. Note that the spatial position relationship between the target (wall) and the robot trajectory can be obtained after floor plan imaging. Thus, the **intuition** on contour splicing is that we can splice targets' contour lines extracted from image profiles based on the temporal relationship of their corresponding motion trajectories to obtain a complete floor plan.

Specifically, since the robot moves constantly in straight lines, we acquire the coordinates of trajectories by estimating the moving distance and moving direction of uniform rectilinear motion segments in time sequence. We collect the angle and acceleration data from the Inertial Measurement Unit (IMU) sensor module equipped on

the mobile robot platform. To identify the uniform rectilinear motion segments of the received signal profiles, we first calculate the sum of the variances of the acceleration measurement values of all axes and find the segment above the predefined threshold. Then we calculate the average angular velocity of this segment which is equal to the total rotation angle divided by the total time. If the average angular velocity is below a threshold, the segment is a uniform rectilinear motion segment, whose starting point and ending point are denoted by st_p and ed_p , respectively. As the moving speed of radar v is known, the moving distance of the segment can be then calculated by $v \cdot (ed_p - st_p)$. And the moving direction value is obtained by averaging all the angle measurements of the uniform rectilinear motion segment. After gathering the 2D coordinates of each trajectory and that of the contour line corresponding to the trajectory, we connect adjacent lines in space and finally obtain a floor plan figure. In most cases, two adjacent contour lines may not be perfectly connected. We further optimize the splicing result. For the parts that cannot be connected, we will extend the two adjacent lines until they are just connected. Our algorithm will also remove the excess.

5 SYSTEM IMPLEMENTATION

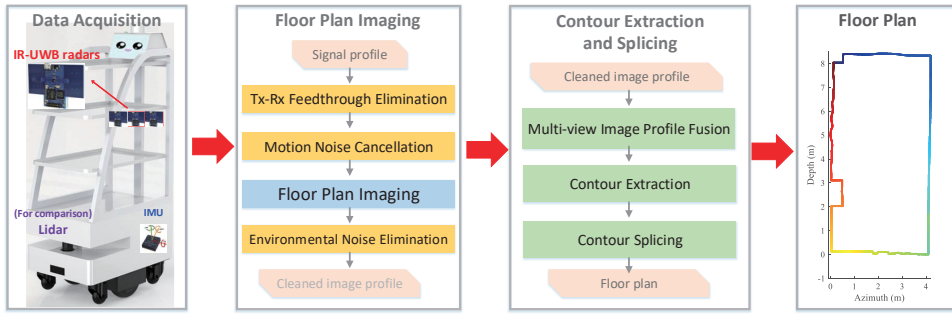


Fig. 12. System overview of UWBMap.

We develop a prototype of UWBMap using off-the-shelf an IR-UWB radar and a commercial mobile robot. As shown in Fig 12, the system consists of three main modules: data acquisition, floor plan imaging and multi-view based contour line extraction and splicing.

For data acquisition, UWBMap adopts 3 COTS impulse radio XETHRU model X4M200 which has a highly integrated X4 system-on-chip [6]. As shown in Fig. 12, each radar has one transmitting antenna and one receiving antenna embedded into a $6.6 \times 4.2\text{cm}^2$ PCB board. The radar transmits pulses with a width of 0.4ns . The center frequency of the radio is 7.29GHz and the bandwidth is 1.4GHz . Benefit from the high-speed analog-to-digital module, the radar receiver samples reflected signals at a frequency of 23.328GS/s , covering a consecutive range of 9.9m . We set frame per seconds as 100. The radars are deployed at a height of about 0.7m from the ground and transmits data to the laptop through a USB port. We use a commercial Reeman mobile robot [36] to navigate indoors. The robot is equipped with an IMU and a laser SLAM module, providing angle and acceleration information and floor plan scanned by Lidar. We use a Python program to control data acquisition of radar and IMU module, and robot movement (i.e., moving speed, direction, and distance). The robot is pre-programmed in the way that it moves forward at a constant speed (0.1m/s to 1m/s), and it will try other directions when an obstacle is ahead. This rule is widely used for commercial robots. The default moving speed of the robot is 0.3m/s . In addition, to avoid the interference of the devices' Tx-Rx Feed-through, we recommend that the radar has a certain distance from the wall, such as 0.3m in our system.

UWBMap has no special requirements and restrictions on the length, and joint angle of wall segments. The floor plan imaging module uses the received signal profiles as input. The angle and acceleration measurements

from the IMU module are adopted to identify the uniform rectilinear motion segments of the received signal profiles. For the multi-view based contour line extraction and splicing module, the input is the clean image profiles of all the radar devices from different views. We also use the angle data of the IMU module to identify the moving direction of the robot. By mapping the extracted contour lines of different trajectories from the image profiles with the correct spatial positions, we obtain the denoised and accurate floor plan. Both the imaging algorithm and the contour line extraction and splicing algorithm are implemented in Matlab.

6 EVALUATION

As shown in Fig. 13, we use five typical indoor scenarios with diversity in our campus building for our evaluation, i.e., a big room ($8.1 \times 8.25m^2$), a medium room ($8.29 \times 4.14m^2$), a small elevator room ($2.35 \times 4.15m^2$), an elevator hall ($8.65 \times 13.49m^2$) and a corridor (about $1.8m$ wide and $16m$ long). Each scenario contains different imaging targets, such as solid and hollow walls, doors, lifts, and glass panes. These targets may be composed of different materials, including metal, concrete, wooden, and glass. And also the scenarios involve multiple internal common joints of these target segments combinations.

We now evaluate the performance of UWBMap both qualitatively and quantitatively. For quantitative assessment, we collect both the ground truth manually and the floor plan created by Lidar for comparison. To obtain the contour line from the floor plan by Lidar, we first perform the morphological operation in image processing on floor plan to obtain the skeleton image, turning the thick boundaries of the image into thin lines. We then detect contour lines based on Hough transform [17]. To determine the 2D coordinates of each contour point, we calculate the scale factor by measuring an object with a specific length. As shown in Fig. 15b, we extract contour lines (the right figure) from the floor plan (the left figure) produced by Lidar. We rotate the contour lines obtained from Lidar and IR-UWB radar to the same direction as the ground truth lines and sample the result produced by two devices with more points to ensure that the number of sample points is basically the same. The error of each contour point is the minimum Euclidean distance between the estimated point and the ground truth line.

6.1 Overall Performance

To evaluate the performance of UWBMap, we conduct experiments in five scenarios. In each scenario, the robot will move along different trajectories at a constant speed of $0.3m/s$. The overall performance in five scenarios is shown in Fig. 14. We can see that IR-UWB achieves comparable performance to Lidar with a median error of $11cm$ and a 90-percentile error of $26cm$. To demonstrate the performance of UWBMap more intuitively, the ground truth and the results from different scenarios are shown in Fig. 15 to Fig. 19.

The ground truth and results of first two rooms are shown in Fig. 15 and Fig. 16. Although IR-UWB radar and Lidar show a similar CDF error trend, we observe big errors for Lidar, as shown on the bottom corner in Fig. 15b. This is because Lidar does not work on glass objects. It is worth noting that although the whole bottom edge is glass, it is interesting that the middle area of the contour can still be detected by Lidar because the middle is covered with stains and dust.



Fig. 13. Five indoor environments for evaluation.

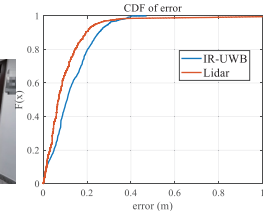


Fig. 14. Overall performance.

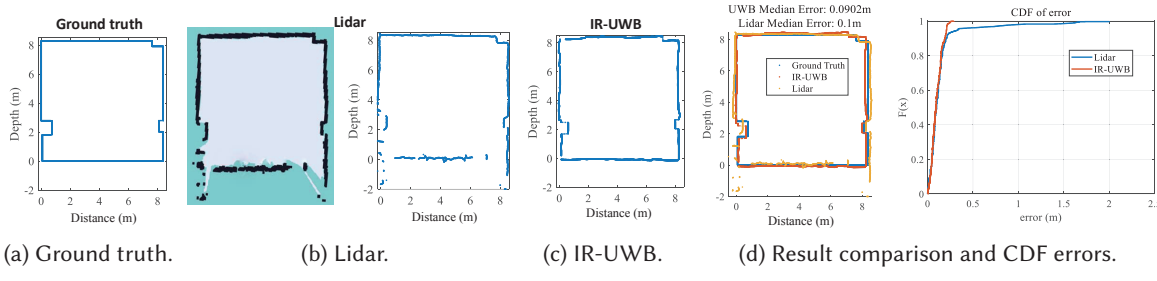


Fig. 15. Experiments in the big room.

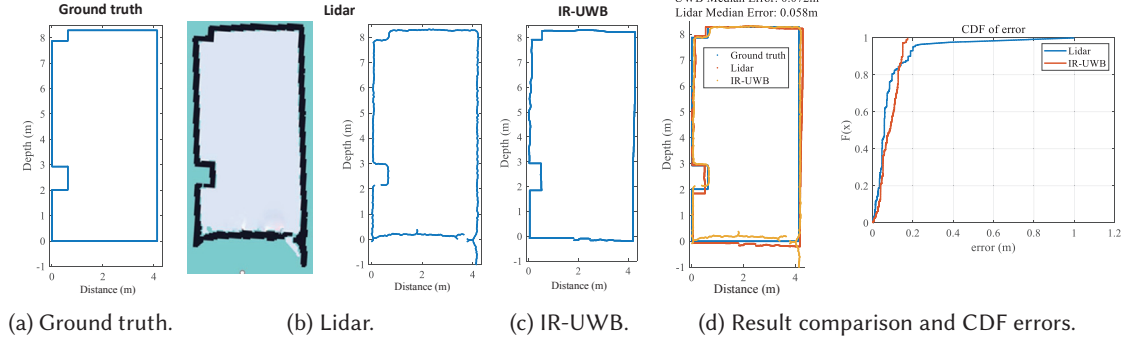


Fig. 16. Experiments in the medium room.

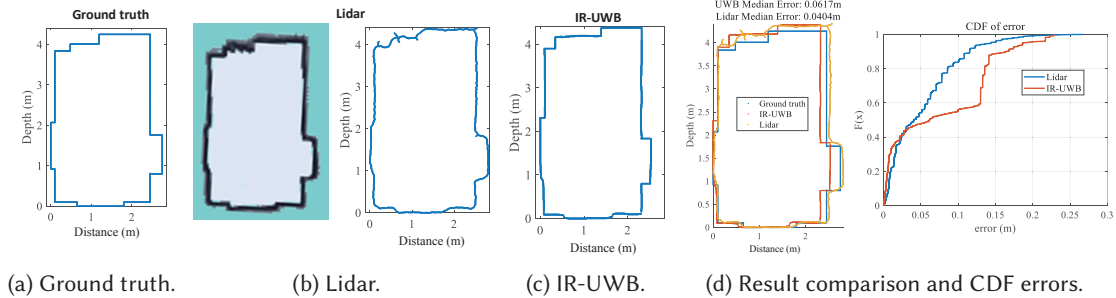


Fig. 17. Experiments in the small elevator room.

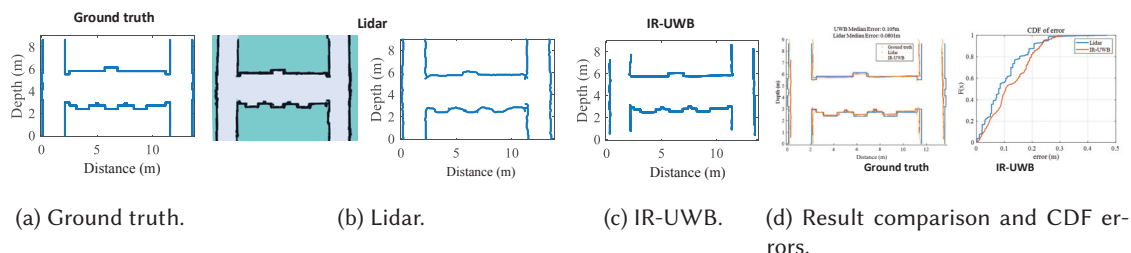


Fig. 18. Experiments in the elevator hall.

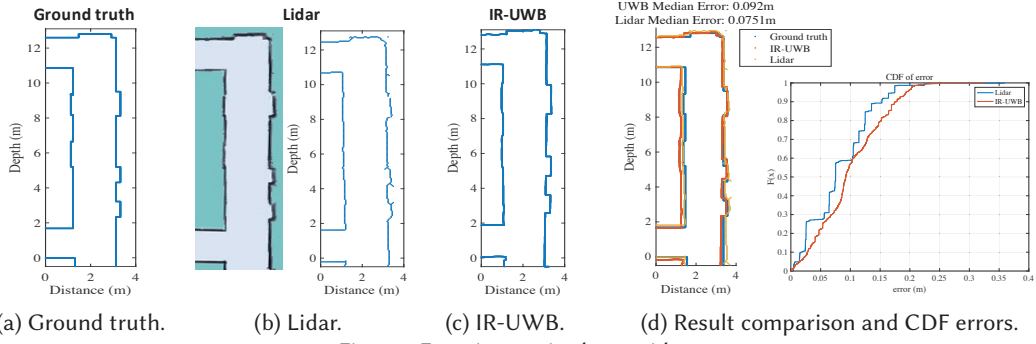


Fig. 19. Experiments in the corridor.

Fig. 17 shows the ground truth and results of the elevator room. It can be seen from Fig. 17d that the shape and length of the contour of IR-UWB show a large deviation from the ground truth, especially for the top edge and the right edge. This is probably because the elevator room in Fig. 17 is small, which limits horizontal movements of the robot. Therefore, the length of the synthetic aperture of IR-UWB is short, inducing imperfect construction results compared with the first two scenarios. We also observe that the top-left corner of the Lidar contour line is messy. It may be due to the existence of a transparent fire hydrant box with three fire extinguishers inside.

In Fig. 18 and 19, the ground truth and results of the elevator hall and corridor are shown. We can see that the CDFs of the errors of UWBMap are comparable to that of Lidar. From Fig. 13, there are two trash bins between every two elevator doors. Fig. 18 shows that both Lidar and UWBMap accurately identify the outlines of these two bins, demonstrating the capability of UWBMap to construct detailed contour lines of indoor layouts.

6.2 Evaluation in Smoke Environments

Disaster events often come with Airborne obscurants such as heavy fog and smoke. To evaluate the operation of UWBMap in emergency events, we conduct experiments in the medium room shown in Fig. 16. We use a smoke generator to generate different density levels of smoke (i.e., thin, light, medium, and heavy), as shown in Fig. 20. We collect data from the robotic platform for both Lidar and UWBMap. The results are shown in Fig. 22b and Fig. 21. In Fig. 22b, UWBMap achieves similar performance in all the four scenarios with different levels of smoke

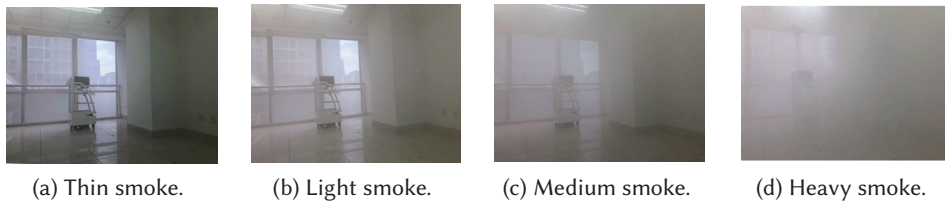


Fig. 20. Qualitative testing in smoke-filled environments

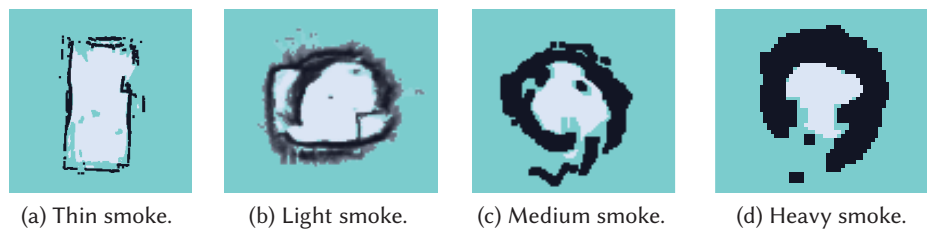


Fig. 21. Experiments in smoke-filled environments.

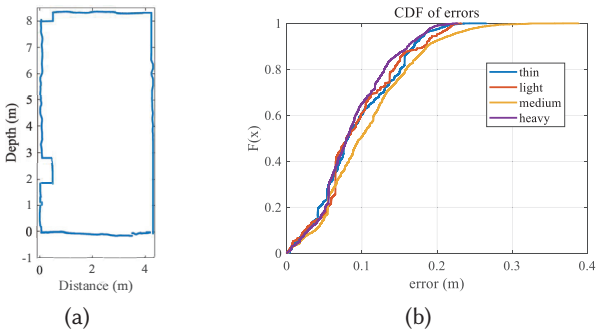


Fig. 22. (a)IR-UWB generated Floor plan in dense smoke scenario. (b)Error CDFs for all the smoke-filled environments.

distributions, demonstrating its ability through smoke. However, in Fig. 21, Lidar performs poorly even the smoke is extremely thin. Fig 21b, 21c, and 21d show a similar round shape with different smoke density levels. This is probably because Lidar scan only detects smoke within a certain radius. The higher the smoke density level is, the shorter the distance is detected. As shown in Fig. 21d, Lidar is completely lost in a heavy smoke condition.

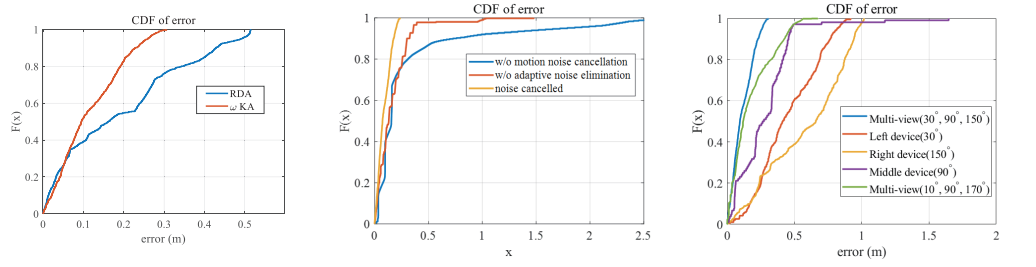
6.3 Effectiveness of Sub-components

In addition to the overall performance, we also evaluate the effectiveness of each component in UWBMMap. We evaluate three main modules—the floor plan imaging algorithm, the noise cancellation method, and the multi-view fusion method.

6.3.1 Effectiveness of Imaging Algorithm. In addition to the ωK algorithm we use, Range-Doppler Algorithm (*RDA*) [13] is one of the most well-known SAR imaging algorithms. We compare the performance of *RDA* to ωKA . The result is shown in Fig. 23a. We observe that ωKA demonstrates better overall performance than *RDA* while part of the errors is close. After analyzing the data, we observe that *RDA* appears horizontal side slopes in the image profile. These side slopes don't affect the imaging result much when the layout (such as the wall) is parallel to the moving trajectory of the radar. However, when layout contour is more complex or has a big inclination angle with respect to the trajectory, affected by the side slopes, the estimated contour lines of *RDA* show big deviation to the ground truth.

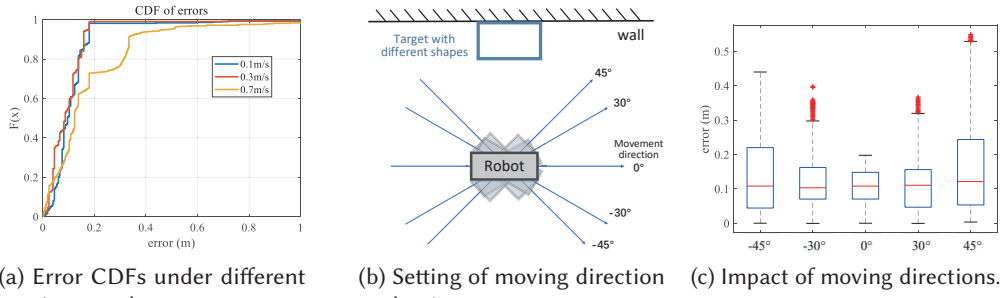
6.3.2 Effectiveness of Noise Cancellation. Note that the noise cancellation module is composed of the motion noise cancellation and environmental noise elimination (adaptive floor plan extraction), and we evaluate each of them. As we can see from Fig. 23b, without motion noise cancellation, many abnormal points with large errors appear. This is because robot bumps while moving may lead to inaccurate range measurements of the target, hence signal profiles after imaging are out of focus and have a big difference from the ideal result. Thus, we cannot extract correct contour lines from distorted images. To evaluate the effectiveness of adaptive noise elimination, we compare our method with the traditional threshold-based method, which eliminates image points whose power is below the fixed threshold from the profiles. Fig. 23b shows that the method we use can effectively eliminate noise interference and extract the effective image of targets from the imaging profile.

6.3.3 Effectiveness of Multi-view Fusion. To evaluate the effectiveness of multi-view fusion, we use the data collected in the medium room shown in Fig. 13. We compare the floor plan results of the different single views (30° , 90° and 150°) with their multi-view result. We also compare different multi-views combinations ($(30^\circ, 90^\circ, 150^\circ)$ and $(10^\circ, 90^\circ, 170^\circ)$). The results are shown in Fig. 23c. On one hand, due to the viewing angles of multiple radars complement well with each other, multi-view based methods work better than that of a single radar, achieving median errors of about 0.1m. And it is worth noted that the middle device in purple shows small errors



(a) Error CDFs for two imaging algorithms. (b) Effectiveness of noise cancellation. (c) Effectiveness of multi-view fusion.

Fig. 23. Evaluation results of sub-components.



(a) Error CDFs under different moving speeds. (b) Setting of moving direction evaluation. (c) Impact of moving directions.

Fig. 24. System robustness under different robot motion states.

than both the left and right devices. This is because the middle device has a wider effective observation angle. No matter which direction the target appears (such as directly in front, left, or right), the radar always has a good chance of observing it. On the other hand, when we use multiple radars, combining different views, the performance doesn't have much difference. This indicates a large selection space of complementary viewing angle combinations.

6.4 System Robustness under Different Robot Motion States

When the sensing target is determined, different movement speeds and movement directions may affect the performance of UWBMap. In this section, we conduct experiments to explore the impact of moving speed and direction. Instead of scanning the entire room, we select a wall and a corner as the background targets and place cupboards with different shapes. We stick tin foil to cupboards with a different shape, i.e., triangle, square, and circle.

6.4.1 Impact of Moving Speed. We program the robot platform to move constantly at three speeds, i.e., 0.1m/s, 0.3m/s, and 0.7m/s, respectively. We plot the CDF of errors in Fig. 24a. Compared with 0.1m/s and 0.3m/s, moving at 0.7m/s generates a larger error due to larger acceleration during start and stop, but the error is very close to the median error of the other two speeds. This experiment demonstrates that the speed of movement doesn't have much effect on UWBMap. As long as the radar is moved at a constant speed, UWBMap can produce floor plan with good quality.

6.4.2 Impact of Moving Directions. Considering the limitation of robot direction under harsh conditions, as shown in Fig. 24b, we evaluate the impact of moving directions with 5 different angles of trajectory. The moving direction parallel to the target (such as the wall) is defined as 0°. Although results from all the directions exhibit close median values, moving directions still have a great impact on system performance. When the radar moves

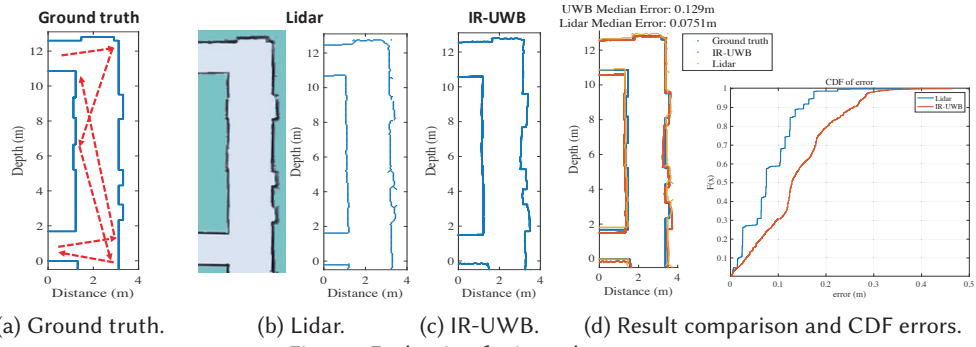


Fig. 25. Evaluation for irregular route 1.

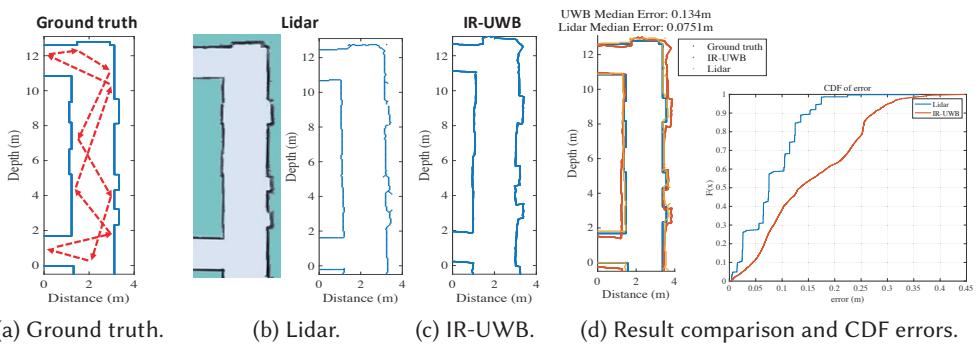


Fig. 26. Evaluation for irregular route 2.

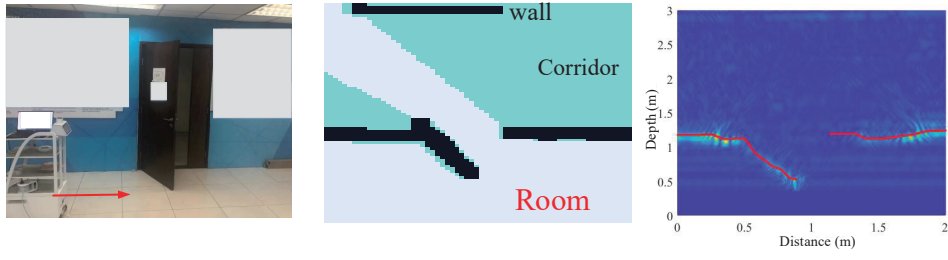
along the 0° trajectory, the radar can evenly receive the echoes from all surfaces of the object. The more the radar is parallel to the sensing target, the better the effect of the floor plan construction is achieved.

6.5 System Performance with Irregular Robot Routes

Note that we splice the contour lines of a floor plan based on their corresponding trajectories of certain moving signal segments. Different robot trajectories (routes) may lead to different floor plan construction results. We randomly generated two irregular paths of the corridor shown in Fig. 13e. As shown in Fig. 25a and Fig. 26a, the ground truth of the floor plan is in blue and the red arrows show the paths. The two routes are irregular in shape and have different distances from the walls. We also show the results of Lidar and IR-UWB, and demonstrate the result comparison and CDF errors of the two routes in Fig. 25 and Fig. 26. We can see that both the shape and length of contour lines produced by UWBM are all similar to the ground truth. The median errors of two irregular routes are 12.9cm and 13.4cm, respectively. Although compared with the route that most of the paths are parallel to the wall (shown in Fig. 19), the performance drops when robot routes are irregular, but on average we still achieve good performance with a median error of 13.1 cm. The main reason for performance degradation is mainly because when the path is not parallel to the wall, the beam center area of at least one device may not cover the wall and the radars cannot evenly receive the echoes from all surfaces of the targets. Thus, the energy of partial target in the multi-device synthesized image profile is relatively low, so that a lot of detailed contour information may be lost during contour extraction. The larger angle between the radar beam center and the target, the large errors usually occur.

6.6 Examples of Partial Layouts

In this experiment, we use UWBM to scan partial layouts. Fig. 27 and Fig. 28 shows the results of an open door and an indoor corner, respectively. In Fig. 27a, the robot moves in a straight line from the left to the right. The



(a) Scenario of an open door.

(b) Lidar results.

(c) IR-UWB results.

Fig. 27. Evaluation for an open door.



(a) Scenario of indoor corner.

(b) Lidar results.

(c) IR-UWB results.

Fig. 28. Evaluation for an indoor corner.

door opens 45° to the inside of the room, and outside the room is a corridor that is about $1.8m$ wide. According to the contour extraction principle of our system, if the depth changes of adjacent wall segments in the image profile is greater than a certain threshold (such as $1.5m$), we consider that the distant segment does not belong to the floor plan of the current room. Therefore, only extract the contour lines of the room are extracted. Fig. 27c and Fig. 28c demonstrate the image profiles and extracted contour lines in red color processed by UWBMap. We observe that the red contour lines are similar to the black lines in the floor plan (Fig. 27b and Fig. 28b) produced by Lidar.

7 DISCUSSION

7.1 Sensing Range

UWB operates through a wide range of low-powered radio frequencies. According to the Federal Communications Commission rules, the maximum allowable power spectral density for UWB transmission is $41.3dBm/MHz$, this corresponds to an average transmit power of $0.5mW$ approximately across the entire band of $3.1 - 10.6GHz$. As such, this limits the maximum sensing range to some extent. On the other hand, due to an effect of strong Tx-Rx feed-through starting at range bin 0, the minimum sensing range is required. Our current prototype performs the best in a range between $0.3m$ to $7m$, applicable for most the indoor environments.

7.2 Material Limitation

Different materials have different reflection and absorption coefficients. In typical indoor environments, concrete, metal, wood and glass are commonly used as wall materials which represent strong reflected signals. Materials such as paper, styrofoam and plastic may have weak reflected signals due to absorption and penetration, therefore our system may not work for these materials.

7.3 Target Complexity

Due to the limitation of image resolution and the over-smoothing effect during feature processing, our system may loss fine-grained target features such as the uneven wall surface. While the proposed system aims for floor plan construction with a focus on wall segments, it can be applied to construct household objects and furniture. These targets may vary in material, shape and size, resulting in complex reflection characteristics than walls. This requires further studies which we leave for our future work.

8 RELATED WORK

8.1 Floor Plan Construction

Floor plan construction (a.k.a. indoor mapping) plays an important role in location-based services and emergency response. Most systems require expensive and special hardware (e.g., Lidar [45], depth cameras [28, 51] and laser rangers [44]). According to a report from Velodyne Lidar [29], a 64-line Lidar unit is priced at US\$70,000 to US\$80,000. The relative cheap single VLP 16-line radar still costs US\$4,000 to US\$8,000. Despite high cost, LiDAR is unable to detect objects behind smoke, fog or dust. RGB-camera based approaches have advantages of low cost and easy use. Existing work [18, 19] generate building interiors by vision based processing, however vision processing is expensive and vision systems have risk of privacy leakage and environmental limitations such as lighting sensitivity (darkness and glare) and blurry images. Acoustic devices such as speaker and microphones [32, 53] have been also explored for indoor mapping, but their performance is restricted by limited sensing range (usually below 2m), noisy environment and sound-absorbing materials. Recently, radio frequency (RF) based approaches are emerging due to its strong penetration under various scenarios. MilliMap [30] presents a single-chip millimetre wave (mmWave) radar based indoor mapping system. It reconstructs dense grid maps through neural networks with conditional generative adversarial network (GAN). Although the results show promising, they require collection of a large amount of training data which is very costly. MILLIPOINT [34] employs a FMCW mmWave radar (i.e., TI AWR1642) to generate point cloud, and produce indoor layout mapping. However, due to its high frequency and short wavelength, mmWave radar signal experiences serious attenuation through walls, hence has weaker penetrability. IR-UWB radar with a lower frequency band (i.e., 3.1GHz-10.6GHz) has been a promising solution. Early UWB based floor plan construction solutions [27, 43] employ military-grade devices, which are heavy and expensive. Le et al. [27] deploy this radar on vehicle with a large antenna array and high transmitting power, and scan indoor layout from outside. However, this system cannot be used indoors. Compared with the existing works, we use low-cost and low-power IR-UWB radar, and overcome the low angle resolution of wide beam, environment noise and limited sensing view by combining multiple devices amounted on mobile robotic platforms. Our system achieves a comparable accuracy to Lidar without smoke, but significantly outperforms Lidar under smoke.

8.2 IR-UWB Based Sensing Applications

In addition to WiFi [46, 49, 50], 4G/5G [9], and FMCW [1] based solutions, UWB radar has been widely used for vital sign monitoring, activity recognition and human tracking. V2iFi [52] utilizes a low-cost UWB to monitor human respiration and heartbeat in vehicle. Using the same device, Multi-Breath [48] transforms the UWB radar signal matrices of different persons as separate RGB images to monitor multi-target respiration. This radar can also be employed to detect the fine-grained movements (e.g., audio vibrations [47]). With fixed multiple UWB radars, Ahmed et al. [2] recognizes eight hand gesture with an accuracy of 95%. Skaria et al. [41] further apply deep-learning techniques for analyzing radar signatures. The signatures of 14 different hand-gestures are passed to a convolutional neural network (CNN) to extract unique features. For coarse-grained movements, HAR-SAnet [11] proposes a UWB based human activity recognition (HAR) system. It adopts an original signal adapted convolutional neural network architecture instead of feeding the handcraft features of RF signals into a

classifier. Seven commonly seen activities (including bending, falling, lying down, standing up, sitting down, squatting down, and walking) are classified with an accuracy of 97.4%. For a specific activity, IR-UWB radar has been employed with a focus on understanding human walking patterns [5]. Rana et al. extract doppler shifts of an individual's gait trait from the associated biomechanical activity and differentiates lower limb movement patterns from other body areas via a radar transceiver. In addition, many existing works adopt lightweight and low-cost off-the-shelf UWB radar devices for human detection and tracking. Singh et al. [40] use a mono-static UWB radar to detect a stationary human target behind a wall based on breathing movements. Kilic et al. [26] develop a training-free indoor UWB device-free person detection and ranging technique by exploiting the temporal variations in the received signal induced by the presence of the person. As for moving target tracking, considering the impact of the target number, clutter and temporary occlusions, Chang et al. [8] presents a multiple hypothesis tracking framework for tracking the ranges and velocities of a variable number of moving human targets via a monostatic UWB radar. Gulmezoglu et al. further apply Gaussian mixture PHD filters to UWB multi-person tracking. The system utilizes four UWB sensors for tracking two moving people in an open indoor scene, achieving a tracking accuracy of 0.25m [21, 22]. Qian et al. proposes the Path-Loss-based Adaptive JPDA (PLA-JPDA) algorithm for indoor multi-person tracking using IR-UWB radars, which can suppress multipath clutter according to the distance-dependent path-loss of radar signals [33].

Since UWB signals have a lower frequency (e.g. 3.1-10.6GHz) and a longer wavelength, it has good performance in penetration. IR-UWB radars have been used in sensing through-the-wall imaging of building interior. Le et al. [27] rely on the military low-frequency radar with specialized antennas or antenna arrays to obtain the distance and angle information of the indoor layout from two sides of the building. The military-grade radar is huge and heavy, hence it is obviously not feasible to use in indoor environments. In recent years, researchers apply civilian radar systems, such as smaller self-made radars, to indoor floor plan construction. Deissler et.al show the possibility of reconstructing the basic features of an indoor environment with a bat-type UWB radar by a combination of an Extended Kalman Filter and a particle filter [14]. Guerra et.al perform indoor mapping was performed using the acquired data while manually rotating a single UWB radar sensor in 45-degree increments [20]. In addition, to find the angle information of the indoor target for the SLAM, Schouten et.al proposed a method of sequentially transmitting UWB pulses with three different center frequencies [38]. Recently, Schouten et.al proposed a method for obtaining spatial information of objects by using two receiving antennas in different directions [39]. However, since the cost of these systems is not low, it is difficult to deploy them widely. And there is still a big gap between the floor plan constructed by these works and the real scene, missing lots of detail contour information.

9 CONCLUSION

In this paper, we present the design and implementation of UWBMap, which is a low-cost floor plan construction system using mono-static IR-UWB radars. From our empirical studies, we discover several key challenges including weak directivity, strong noise interference and limited observation view in the process of IR-UWB based floor plan construction. A series of techniques are proposed to tackle these challenges. Our evaluation results show the promise of our system, outperforming Lidar based solutions. For our future work, we plan to explore the capability of our system in other specific applications, such as indoor localization, navigation, and enriching location-based services. We also plan to evaluate our system performance in more complicated indoor environments, such as an apartment with different types of household objects and furniture.

ACKNOWLEDGMENTS

This work is supported by the National Natural Science Foundation of China A3 Foresight Program (No.62061146001), the National Natural Science Foundation of China (No. 62172394, No. 61802373), the PKU-Baidu Fund (No.

2019BD005), the HUAWEI-PKU collaboration project, the PKU-NTU collaboration Project, the Youth Innovation Promotion Association, Chinese Academy of Sciences (No. 2020109), the EU Horizon 2020 research and innovation programme IDEA-FAST (No. 853981) , and the EU CHIST-ERA RadioSense Project.

REFERENCES

- [1] Fadel Adib, Zach Kabelac, Dina Katabi, and Robert C Miller. 2014. 3d tracking via body radio reflections. In *11th {USENIX} Symposium on Networked Systems Design and Implementation ({NSDI} 14)*. 317–329.
- [2] Shahzad Ahmed and Sung Ho Cho. 2020. Hand gesture recognition using an IR-UWB radar with an inception module-based classifier. *Sensors* 20, 2 (2020), 564.
- [3] Mostafa Alizadeh, George Shaker, João Carlos Martins De Almeida, Plinio Pelegrini Morita, and Safeddin Safavi-Naeini. 2019. Remote monitoring of human vital signs using mm-Wave FMCW radar. *IEEE Access* 7 (2019), 54958–54968.
- [4] Nikolaj Andersen, Kristian Granhaug, Jørgen Andreas Michaelsen, Sumit Bagga, Håkon A Hjortland, Mats Risopatron Knutsen, Tor Sverre Lande, and Dag T Wisland. 2017. A 118-mW pulse-based radar SoC in 55-nm CMOS for non-contact human vital signs detection. *IEEE Journal of Solid-State Circuits* 52, 12 (2017), 3421–3433.
- [5] Boyd Anderson, Mingqian Shi, Vincent YF Tan, and Ye Wang. 2019. Mobile Gait Analysis Using Foot-Mounted UWB Sensors. *Proceedings of the ACM on Interactive, Mobile, Wearable and Ubiquitous Technologies* 3, 3 (2019), 1–22.
- [6] Novelda AS. 2021. X4 - Datasheet. https://www.radartutorial.eu/19.kartei/13.labs/pubs/x4_datasheet_revE_restricted.pdf.
- [7] Glenn D Boreman. 2001. *Modulation transfer function in optical and electro-optical systems*. Vol. 4. SPIE press Bellingham, WA.
- [8] SangHyun Chang, Rangoli Sharan, Michael Wolf, Naoki Mitsumoto, and Joel W Burdick. 2010. People tracking with UWB radar using a multiple-hypothesis tracking of clusters (MHTC) method. *International Journal of Social Robotics* 2, 1 (2010), 3–18.
- [9] Weiyan Chen, Kai Niu, Deng Zhao, Rong Zheng, Dan Wu, Wei Wang, Leye Wang, and Daqing Zhang. 2020. Robust dynamic hand gesture interaction using LTE terminals. In *2020 19th ACM/IEEE International Conference on Information Processing in Sensor Networks (IPSN)*. IEEE, 109–120.
- [10] Yuwei Chen, Jian Tang, Changhui Jiang, Lingli Zhu, Matti Lehtomäki, Harri Kaartinen, Risto Kaijaluoto, Yiwu Wang, Juha Hyypää, Hannu Hyypää, et al. 2018. The accuracy comparison of three simultaneous localization and mapping (SLAM)-based indoor mapping technologies. *Sensors* 18, 10 (2018), 3228.
- [11] Zhe Chen, Chao Cai, Tianyu Zheng, Jun Luo, Jie Xiong, and Xin Wang. 2021. RF-Based Human Activity Recognition Using Signal Adapted Convolutional Neural Network. *IEEE Transactions on Mobile Computing* (2021).
- [12] Kok Seng Chong and Lindsay Kleeman. 1999. Feature-based mapping in real, large scale environments using an ultrasonic array. *The International Journal of Robotics Research* 18, 1 (1999), 3–19.
- [13] Ian G Cumming and Frank H Wong. 2005. Digital processing of synthetic aperture radar data. *Artech house* 1, 3 (2005).
- [14] Tobias Deissler and Jörn Thielecke. 2009. Feature based indoor mapping using a bat-type UWB radar. In *2009 IEEE International Conference on Ultra-Wideband*. IEEE, 475–479.
- [15] Sedat Dogru and Lino Marques. 2019. Using radar for grid based indoor mapping. In *2019 IEEE International Conference on Autonomous Robot Systems and Competitions (ICARSC)*. IEEE, 1–6.
- [16] Jiang Dong, Yu Xiao, Marius Noreikis, Zhonghong Ou, and Antti Ylä-Jääski. 2015. iMoon: Using smartphones for image-based indoor navigation. In *Proceedings of the 13th ACM Conference on Embedded Networked Sensor Systems*. 85–97.
- [17] Richard O Duda and Peter E Hart. 1972. Use of the Hough transformation to detect lines and curves in pictures. *Commun. ACM* 15, 1 (1972), 11–15.
- [18] Ugur Murat Erdem and Stan Sclaroff. 2003. Automated placement of cameras in a floorplan to satisfy task-specific constraints. *Boston University, Boston December 2003* (2003).
- [19] Ruipeng Gao, Mingmin Zhao, Tao Ye, Fan Ye, Yizhou Wang, Kaigui Bian, Tao Wang, and Xiaoming Li. 2014. Jigsaw: Indoor floor plan reconstruction via mobile crowdsensing. In *Proceedings of the 20th annual international conference on Mobile computing and networking*. 249–260.
- [20] Anna Guerra, Francesco Guidi, Lilia Ahtaryieva, Nicoló Decarli, and Davide Dardari. 2016. Crowd-based personal radars for indoor mapping using UWB measurements. In *2016 IEEE International Conference on Ubiquitous Wireless Broadband (ICUWB)*. IEEE, 1–4.
- [21] Berk Gülmezoglu. 2014. *Indoor multi-person tracking via ultra-wideband radars*. Ph.D. Dissertation. bilkent university.
- [22] Berk Gulmezoglu, Mehmet Burak Guldogan, and Sinan Gezici. 2014. Multiperson tracking with a network of ultrawideband radar sensors based on Gaussian mixture PHD filters. *IEEE Sensors Journal* 15, 4 (2014), 2227–2237.
- [23] Apple Inc. 2021. Ultra wideband availability - Apple support. <https://support.apple.com/en-us/HT212274>.
- [24] Texas Instruments. 2021. AWR1443. <https://www.ti.com/product/AWR1443>.
- [25] Texas Instruments. 2021. AWR1642. <https://www.ti.com.cn/product/AWR1642>.
- [26] Yakup Kılıç, Henk Wymeersch, Arjan Meijerink, Mark J Bentum, and William G Scanlon. 2013. Device-free person detection and ranging in UWB networks. *IEEE journal of selected topics in signal processing* 8, 1 (2013), 43–54.

- [27] Calvin Le, Traian Dogaru, Lam Nguyen, and Marc A Ressler. 2009. Ultrawideband (UWB) radar imaging of building interior: Measurements and predictions. *IEEE Transactions on Geoscience and Remote Sensing* 47, 5 (2009), 1409–1420.
- [28] Phi-Hung Le and Jana Košecka. 2017. Dense piecewise planar RGB-D SLAM for indoor environments. In *2017 IEEE/RSJ International Conference on Intelligent Robots and Systems (IROS)*. IEEE, 4944–4949.
- [29] Velodyne Lidar. 2021. Velodyne lidar. <https://velodynelidar.com/products/>.
- [30] Chris Xiaoxuan Lu, Stefano Rosa, Peijun Zhao, Bing Wang, Changhao Chen, John A Stankovic, Niki Trigoni, and Andrew Markham. 2020. See through smoke: robust indoor mapping with low-cost mmWave radar. In *Proceedings of the 18th International Conference on Mobile Systems, Applications, and Services*. 14–27.
- [31] Alberto Moreira, Pau Prats-Iraola, Marwan Younis, Gerhard Krieger, Irena Hajnsek, and Konstantinos P Papathanassiou. 2013. A tutorial on synthetic aperture radar. *IEEE Geoscience and remote sensing magazine* 1, 1 (2013), 6–43.
- [32] Swadhin Pradhan, Ghulfran Baig, Wenguang Mao, Lili Qiu, Guohai Chen, and Bo Yang. 2018. Smartphone-based acoustic indoor space mapping. *Proceedings of the ACM on Interactive, Mobile, Wearable and Ubiquitous Technologies* 2, 2 (2018), 1–26.
- [33] Hongyu Qian, Xizhu Yang, Xinyue Zhang, Yi Ding, and Lin Zhang. 2020. PLA-JPDA for Indoor Multi-Person Tracking Using IR-UWB Radars. In *2020 IEEE Radar Conference (RadarConf20)*. IEEE, 1–6.
- [34] Kun Qian, Zhaoyuan He, and Xinyu Zhang. 2020. 3D Point Cloud Generation with Millimeter-Wave Radar. *Proceedings of the ACM on Interactive, Mobile, Wearable and Ubiquitous Technologies* 4, 4 (2020), 1–23.
- [35] S Quegan. 1997. Spotlight Synthetic Aperture Radar: Signal Processing Algorithms. *Journal of Atmospheric and Solar-Terrestrial Physics* 59 (1997), 597–598.
- [36] Reeman Robot. 2021. Reeman robot. <https://www.reeman.cn/products/robot/trooper>.
- [37] SamMobile. 2021. Samsung explains the uses of Galaxy Note 20's UWB feature in new video. <https://www.sammobile.com/news/samsung-explains-galaxy-note-20-uwb-feature-video/>.
- [38] Girmi Schouten and Jan Steckel. 2017. RadarSLAM: Biomimetic SLAM using ultra-wideband pulse-echo radar. In *2017 International Conference on Indoor Positioning and Indoor Navigation (IPIN)*. IEEE, 1–8.
- [39] Girmi Schouten and Jan Steckel. 2019. A biomimetic radar system for autonomous navigation. *IEEE Transactions on Robotics* 35, 3 (2019), 539–548.
- [40] Sukhvinder Singh, Qilian Liang, Dechang Chen, and Li Sheng. 2011. Sense through wall human detection using UWB radar. *EURASIP Journal on Wireless Communications and Networking* 2011, 1 (2011), 1–11.
- [41] Sruthy Skaria, Akram Al-Hourani, and Robin J Evans. 2020. Deep-Learning Methods for Hand-Gesture Recognition Using Ultra-Wideband Radar. *IEEE Access* 8 (2020), 203580–203590.
- [42] ClearWay Software and Sensors. 2021. NavTech radar. <https://navtechradar.com/clearway-technical-specifications/>.
- [43] Yongping Song, Jun Hu, Ning Chu, Tian Jin, Jianwen Zhang, and Zhimin Zhou. 2018. Building layout reconstruction in concealed human target sensing via UWB MIMO through-wall imaging radar. *IEEE Geoscience and Remote Sensing Letters* 15, 8 (2018), 1199–1203.
- [44] Hartmut Surmann, Andreas Nüchter, and Joachim Hertzberg. 2003. An autonomous mobile robot with a 3D laser range finder for 3D exploration and digitalization of indoor environments. *Robotics and Autonomous Systems* 45, 3-4 (2003), 181–198.
- [45] Silvia Liberata Ullo, Chiara Zarro, Konrad Wojtowicz, Giuseppe Meoli, and Mariano Focareta. 2020. LiDAR-based system and optical VHR data for building detection and mapping. *Sensors* 20, 5 (2020), 1285.
- [46] Hao Wang, Daqing Zhang, Junyi Ma, Yasha Wang, Yuxiang Wang, Dan Wu, Tao Gu, and Bing Xie. 2016. Human respiration detection with commodity wifi devices: do user location and body orientation matter?. In *Proceedings of the 2016 ACM International Joint Conference on Pervasive and Ubiquitous Computing*. 25–36.
- [47] Ziqi Wang, Zhe Chen, Akash Deep Singh, Luis Garcia, Jun Luo, and Mani B Srivastava. 2020. UWHear: through-wall extraction and separation of audio vibrations using wireless signals. In *Proceedings of the 18th Conference on Embedded Networked Sensor Systems*. 1–14.
- [48] Yanni Yang, Jiannong Cao, Xiulong Liu, and Xuefeng Liu. 2019. Multi-breath: Separate respiration monitoring for multiple persons with UWB radar. In *2019 IEEE 43rd Annual Computer Software and Applications Conference (COMPSAC)*, Vol. 1. IEEE, 840–849.
- [49] Youwei Zeng, Dan Wu, Jie Xiong, Enze Yi, Ruiyang Gao, and Daqing Zhang. 2019. FarSense: Pushing the range limit of WiFi-based respiration sensing with CSI ratio of two antennas. *Proceedings of the ACM on Interactive, Mobile, Wearable and Ubiquitous Technologies* 3, 3 (2019), 1–26.
- [50] Daqing Zhang, Hao Wang, Yasha Wang, and Junyi Ma. 2015. Anti-fall: A non-intrusive and real-time fall detector leveraging CSI from commodity WiFi devices. In *International Conference on Smart Homes and Health Telematics*. Springer, 181–193.
- [51] Ying Zhang, Chuanjiang Luo, and Juan Liu. 2012. Walk&sketch: create floor plans with an rgb-d camera. In *Proceedings of the 2012 ACM Conference on Ubiquitous Computing*. 461–470.
- [52] Tianyue Zheng, Zhe Chen, Chao Cai, Jun Luo, and Xu Zhang. 2020. V2iFi: in-Vehicle Vital Sign Monitoring via Compact RF Sensing. *Proceedings of the ACM on Interactive, Mobile, Wearable and Ubiquitous Technologies* 4, 2 (2020), 1–27.
- [53] Bing Zhou, Mohammed Elbadry, Ruipeng Gao, and Fan Ye. 2017. BatMapper: Acoustic sensing based indoor floor plan construction using smartphones. In *Proceedings of the 15th Annual International Conference on Mobile Systems, Applications, and Services*. 42–55.